İSTANBUL UNIVERSITY
CERRAHPAŞA

ORIGINAL ARTICLE
Electrica 2025; 25: 1-21

Effects of Direct-Quadrature Rotor Current Sensors' Faults in Wind Energy Conversion System based on Doubly Fed Induction Generator

Naziha Chouider[1], Karim Beddek[1], Rezki Haddouche[2], Mohamed Zerrougui[3], Omar Ramdani[1]

[1]Department of Automation and Electrification, Laboratory of Applied Automation, M'Hamed Bougara University of Boumerdes Faculty of Hydrocarbons and Chemistry, Boumerdes, Algeria
[2]Department of Power and Control, Institution of Electrical and Electronic Engineering, M'Hamed Bougara University of Boumerdes, Boumerdes, Algeria
[3]Department of Computer Science and Interaction,Laboratory of Information and System (LIS-Lab UMR CNRS 7020), Aix-Marseille University Faculty of Science, Marseille, France

Cite this article as: N. Chouider, K. Beddek, R. Haddouche, M. Zerrougui and O. Remdani, "Effects of direct-quadrature rotor current sensors' faults in wind energy conversion system based on doubly fed induction generator," *Electrica*, 25, 0042, 2025. doi: 10.5152/electrica.2025.25042.

WHAT IS ALREADY KNOWN ON THIS TOPIC?

- *Wind energy conversion systems based on doubly fed induction generator are popular due to their high efficiency, good control characteristics, and suitability for variable speed operation.*
- *Existing researches and studies mainly focus on how WECSs perform under external faults and disturbances such as grid side faults: voltage dips, short circuits, and wind speed fluctuations.*
- *Many advanced control methods exist for handling these external faults and improving fault ride-through capabilities.*

Corresponding author:
Naziha Chouider

E-mail:
na.chouider@univ-boumerdes.dz

Received: March 5, 2025
Revision Requested: March 21, 2025
Last Revision Received: July 3, 2025
Accepted: July 7, 2025
Publication Date: August 29, 2025

DOI: 10.5152/electrica.2025.25042

ABSTRACT

This paper investigates the dynamic performance of a grid-connected wind energy conversion system (WECS) based on a doubly fed induction generator (DFIG) in the presence of additive and multiplicative faults in direct-quadrature rotor current sensors. The system architecture includes direct current-link voltage regulation, via the grid side converter and active/reactive power control, through the rotor side converter. Unlike prior studies that mainly consider symmetrical grid faults, this work systematically introduces various sensor faults specifically in stator current, stator voltage, and rotor current measurements into the rotor current control loop. The impact of these faults is assessed by examining key electrical parameters such as current, voltage, active, and reactive power across the grid, stator, and rotor. Simulation results reveal that rotor current sensor faults significantly degrade system stability and power regulation. These findings highlight the importance of developing robust fault detection and isolation and fault-tolerant control strategies and provide a foundation for enhancing the reliability of DFIG-based WECS under sensor fault conditions.

Index Terms—Additive and multiplicative faults, doubly fed induction generator (DFIG), grid side converter (GSC), rotor side converter (RSC), sensors , wind energy conversion system (WECS).

I. INTRODUCTION

Concerns about global warming and the objective of reducing dependence on fossil fuels are shifting energy production trends toward renewable energy sources (RESs). Among these, wind energy stands out as one of the most alluring RESs due to its availability, modern technology, dependable infrastructure, cost-effectiveness, and rapid development [1-4]. Among the available technologies, the wind energy conversion system (WECS) based on a doubly fed induction generator (DFIG) has gained prominence for its good performance, high efficiency, improved active and reactive power characteristics, quality, control, and small-sized power converter. One of its additional benefits is its wider power capture capability over a large range of wind speeds [1, 2, 5].

Despite these advantages, WECSs based on DFIG are highly sensitive to both internal and external faults, which can severely compromise system performance and stability, potentially resulting in operational failure and significant economic losses [2, 3]. Internal faults refer to failures within the internal system components, while external faults originate outside the system and manifest as disturbances superimposed on the system. These can gradually lead to degraded energy capture, transient responses, voltage and current imbalances, and increased maintenance costs. Therefore, it is of interest to increase the reliability and security of the WECS.

A substantial body of research has focused on improving doubly fed induction machine (DFIM) control under varying operating conditions. Classical vector control strategies, such as

WHAT DOES THIS STUDY ADD TO THIS TOPIC?

- *This study shifts the focus from external faults, like grid side faults, to internal faults, rotor-side control loop faults, especially in the direct-quadrature rotor current sensors of the DFIG. It provides a deeper investigation of rotor-side sensor faults, which are rarely explored in previous literature.*
- *The paper systematically analyzes how additive and multiplicative faults, both symmetrical and asymmetrical, in rotor current, stator current, and stator voltage sensors affect the WECS-DFIG performance.*
- *Simulation results show significant degradation in rotor stability and power regulation due to direct-quadrature rotor current sensors faults.*
- *The study proposes fault analysis as a foundation for developing fault-tolerant control strategies.*

field-oriented control (FOC) and its variant indirect field-oriented control, have been widely adopted due to their superior dynamic performance and ability to decouple torque and flux control [5-8]. However, their sensitivity to machine parameter variations has prompted the development of direct torque control (DTC) as an alternative [9-11]. Initial DFIG implementations for wind generation by Peña et al. [12, 13] laid the foundation for further modeling and grid interaction studies [14, 15]. Efforts to enhance control performance under unbalanced or faulty grid conditions have also been reported using hysteresis controllers [16, 17], coordinated control loops [18], and advanced feedback linearization [19].

Wind energy conversion system based on DFIG have been extensively studied for their performance improvement during grid disturbances, with significant focus on enhancing fault ride-through (FRT) capabilities and mitigating the impacts of grid faults through advanced control strategies [2, 20]. Sophisticated control methods for the rotor side converter (RSC) have been proposed, including proportional current tracking [21], flux tracking [22], transient feedforward control [23], active damping [24], and robust control techniques [25, 26]. In addition, these papers [27, 28] primarily address external disturbances such as grid faults, wind speed variations, and converter protection mechanisms. Additional work has focused on stabilizing the direct current (DC)-link voltage during grid faults by modifying the RSC control [29] and employing maximum power point tracking (MPPT) techniques like tip-speed ratio control [30], power signal feedback [31], and hill climb search [32].

While extensive research has been conducted on grid-side fault scenarios and corresponding mitigation techniques, relatively few studies have focused on faults within the rotor current control loop, particularly concerning direct-quadrature current sensor faults. This gap is critical, as faults in the direct-quadrature rotor current sensors or controllers can significantly degrade system stability and power quality. Recent advancements have begun to fill this void. Abbas et al. [33] introduced an innovative diagnostic approach utilizing an Extended Kalman Filter bank to detect, locate, and isolate single and multiple phase current sensor faults in both converters of a DFIG-based WECS. Their method effectively estimates converter currents and compares them with sensor measurements to generate residuals for fault identification. Similarly, Mousavi [34] developed a fault-tolerant fractional-order sliding mode controller augmented with state observers to estimate rotor current dynamics during sensor faults, enhancing the system's resilience to such internal anomalies. Further studies have employed signal processing techniques for fault detection. For instance, spectral and wavelet analyses have been utilized to detect inter-turn short-circuit faults in rotor windings by analyzing harmonic frequency components in rotor current signals [35]. Additionally, observer-based methods, such as sliding mode observers, have been proposed for rotor current-based fault detection, offering robustness against system uncertainties and external disturbances [36]. Despite these contributions, the specific impact of direct-quadrature rotor current sensor faults on the performance of the WECS remains insufficiently investigated. Understanding and mitigating these faults are crucial for enhancing the reliability and efficiency of wind energy systems.

This study aims to address this research gap by analyzing the effects of faults in direct-quadrature rotor current control loop sensors. The investigation considers faults arising in stator current, stator voltage, and rotor current sensors. The control design used for this study employs the FOC technique with the aim of adjusting the RSC and the hysteresis control technique with the aim of controlling the grid side converter (GSC). The objective is to evaluate the impact of these faults on the control performance of the WECS, thereby supporting the development of reliable fault-tolerant control (FTC) frameworks. The system's behavior under different fault scenarios is examined through detailed simulation studies. The remainder of this paper is organized as follows: Section II presents the modeling of the wind turbine and the DFIM, along with the design of the control system, focusing on the GSC and RSC controllers. The modeling approach for both additive and multiplicative faults is also described through this section. Section III discusses the interaction between the power system and the WECS based on DFIG under various direct-quadrature rotor current fault conditions, with simulations performed in MATLAB/SIMULINK. The results and their analysis are provided in the same section. Finally, Section IV concludes the paper and outlines potential directions for future research trends in FTC strategies.

II. MATERIALS AND METHODS

The control strategy explored in this study employs vector control (FOC) using a rotating direct-quadrature reference frame aligned with the stator flux. Proportional-integral (PI) controllers regulate the DC-link voltage and the rotor current loops after applying decoupling compensation. Within this framework, the RSC independently regulates the active and reactive power at the DFIG terminals through rotor current control. The GSC, operated with a hysteresis current controller, stabilizes the DC-link voltage and ensures a sinusoidal current injection into the grid. It enables power exchange through the rotor converter while delivering additional reactive power support. Fig. 1 illustrates the schematic diagram of the proposed controlled grid-connected WECS based on DFIG.

A. Description of the Wind Energy Conversion System based on Doubly Fed Induction Generator

1) Wind Turbine Model

The power extracted by a wind turbine and the wind turbine torque are related to the wind speed and can be expressed in (1) and (2), respectively, as follows [1, 37]:

$$P_m = 0.5 C_p(\lambda,\beta)\rho ? r^2 v^3 \tag{1}$$

$$T_m = 0.5 C_t(\lambda,\beta)\rho ? r^3 v^2 \tag{2}$$

where ρ represents the air density, r is the turbine blade radius, and v denotes the wind speed. C_p and C_t are the power and the torque coefficients of the wind turbine, both of which are functions of the tip-speed ratio λ and pitch angle β. The tip speed ratio can be defined as a function of ω (the generator's rotational speed) as illustrated in (3):

$$\lambda = \omega r / v \tag{3}$$

According to (3), adjusting the generator's rotational speed ω allows the control of λ, which in turn affects both coefficients , C_p and C_t, and thus the power generated by the wind turbine.

B. Doubly Fed Induction Generator Model

With a nonzero rotor voltage, the DFIG functions similarly as a conventional induction generator. In a synchronously rotating direct-quadrature reference frame, the dynamic equations of the DFIG stator voltage and rotor circuits can be described through equations from (4.a) to (7.b), which show the relationships between flux, current, and voltage in each axis as follows [38, 39]:

$$v_{ds} = R_s i_{ds} - \omega_s \psi_{qs} + {d\psi_{ds}}/{dt} \tag{4.a}$$

$$v_{qs} = R_s i_{qs} + \omega_s \psi_{ds} + {d\psi_{qs}}/{dt} \tag{4.b}$$

$$v_{dr} = R_r i_{dr} - s\omega_s \psi_{qr} + {d\psi_{dr}}/{dt} \tag{5.a}$$

$$v_{qr} = R_r i_{qr} + s\omega_s \psi_{dr} + {d\psi_{qr}}/{dt} \tag{5.b}$$

$$\psi_{ds} = L_s i_{ds} + L_m i_{dr} \tag{6.a}$$

$$\psi_{qs} = L_s i_{qs} + L_m i_{qr} \tag{6.b}$$

$$\psi_{dr} = L_r i_{dr} + L_m i_{ds} \tag{7.a}$$

$$\psi_{qr} = L_r i_{qr} + L_m i_{qs} \tag{7.b}$$

Here, $\boldsymbol{\omega_s}$ denotes the speed of the synchronous reference frame, $\boldsymbol{s\omega_s = (\omega_s - \omega_e)}$ represents the slip frequency, with $\boldsymbol{s}$ is the slip and $\boldsymbol{\omega_e}$ the generator's electrical speed, related to the mechanical speed through the number of poles, $\boldsymbol{P}$, as: $\omega_e = \frac{P}{2}\boldsymbol{\omega_r}$. Parameters $\boldsymbol{R_s}$, $\boldsymbol{R_r}$, $\boldsymbol{L_s}$, and $\boldsymbol{L_r}$ correspond to the resistances and inductances of the stator and rotor, respectively, while $\boldsymbol{L_m}$ is the mutual inductance and $\boldsymbol{\omega_r}$ represents the rotor's angular speed. The electrical torque produced by the DFIG can be calculated, based on flux and current components, through (8) [39]:

$$T_e = \frac{3}{2}P\left(\psi_{dr} i_{qs} - \psi_{qr} i_{ds}\right) = \frac{3}{2}PL_m\left(i_{dr} i_{qs} - i_{qr} i_{ds}\right) \tag{8}$$

Stator and rotor active and reactive powers, neglecting the power losses associated with the stator and rotor resistances, can be represented in (9.a), (9.b), (10.a), and (10.b), respectively [1, 39, 40]:

$$P_s = \frac{3}{2}\left(v_{ds} i_{ds} + v_{qs} i_{qs}\right) \tag{9.a}$$

$$Q_s = \frac{3}{2}\left(v_{qs} i_{ds} - v_{ds} i_{qs}\right) \tag{9.b}$$

$$P_r = \frac{3}{2}\left(v_{dr} i_{dr} + v_{qr} i_{qr}\right) \tag{10.a}$$

$$Q_r = \frac{3}{2}\left(v_{qr} i_{dr} - v_{dr} i_{qr}\right) \tag{10.b}$$

C. Control System Design

Rotor side converter and GSC together manage the operation of the DFIG. The GSC maintains a steady DC-link voltage, regardless of the rotor power flow's amount and direction [3], and supplies reactive power to the grid. However, the RSC is responsible for active and reactive power regulation [1, 41].

To achieve the GSC's goals, a hysteresis current control approach aligned with the stator voltage vector is implemented, as illustrated through Fig. 2(a). The DC-link voltage serves as the voltage source for the other three-phase converters connected to the rotor winding terminals RSC. Direct current-bus capacitor and pulse width modulation (PWM) converter are employed to eliminate ripple and maintain a steady DC-link voltage successively [1, 42].

Equations (11) and (12) below provide the variation of the voltage at the DC-link*:*

$$e = v_{dc_{ref}} - v_{dc\_measured} \tag{11}$$

$$\Delta e = \left(1 - z^{-1}\right) \tag{12}$$

The voltage direct-quadrature components of the inverter at the grid terminals are given in (13.a) and (13.b) below [38]:

$$v_d = Ri_d + L\frac{di_d}{dt} - L\omega i_q + v_{dl} \tag{13.a}$$

$$v_q = Ri_q + L\frac{di_q}{dt} - L\omega i_d + v_{ql} \tag{13.b}$$

where v_d, v_q, i_d, and i_q represent the direct-quadrature components of the grid inverter voltage and the grid current. L and R corresponds to the filter inductance and resistance, while $\boldsymbol{\omega}$ represents the grid angular frequency. The associated active and reactive power injected into the grid can be expressed by (14.a) and (14.b):

$$P = 3\left(v_d i_d + v_q i_q\right) \tag{14.a}$$

$$Q = 3\left(v_d i_q + v_q i_d\right) \tag{14.b}$$

The angular position of the grid voltage may be achieved through (15):

$$\theta_e = \int \omega_e dt = \tan^{-1} {}^{v_\beta}\!/_{v_\alpha} \tag{15}$$

Where v_α and v_β denote the grid voltage components in (α-β) reference frame.

In a voltage vector-oriented reference frame, the direct current of the grid *id* regulates the *DC-link* voltage. As a result, a reference current *id_ref* is obtained from *e* and its variation Δe through a tuned PI controller, as illustrated in Fig. 1. To achieve unity power factor operation at the GSC, the reactive power is set to zero, aligning the d-axis component of the voltage v_d, $v_q = 0$, making iq_{ref} zero. Following a *dq-abc* transformation of these reference currents, hysteresis modulation is then implemented.

To deliver the required active and reactive power at the stator terminals, the magnetization current waveforms should be provided by the RSC to the rotor. The rotor currents *iabc-r* can be broken down into their direct-quadrature components *idr* and *iqr*. Here, *idr* manages the reactive power that enters the machine, while *iqr* adjusts the active power. By properly adjusting these two current components, the stator's active and reactive power outputs can be accurately controlled.

According to Lenz's law, the stator voltage corresponds to the time derivative of the stator flux linkage, which helps determine the instantaneous position of rotating flux vector and thereby defines the rotating reference frame. The three-phase stator voltages and currents are transformed into their *α-β* components v_α, v_β, i_α, and i_β. In the stationary *α-β* reference frame, the stator flux is determined by (16):

$$\psi_{\alpha\beta s} = \int v_{\alpha\beta s} - R_s i_{\alpha\beta s} dt = \left(\psi_{\alpha s} - \psi_{\beta s}\right) \tag{16}$$

Equations (17), (17.a), and (17.b) below define the instantaneous stator flux angle and its components, which indicates the stator rotating magnetic field position [43]:

$$\psi_s = \left|\psi_{\alpha\beta s}\right| angle\left(\psi_{\alpha\beta s}\right) \tag{17}$$

$$angle\left(\psi_{\alpha\beta s}\right) = \theta_s = \tan^{-1}\left(\frac{\psi_{\alpha s}}{\psi_{\beta s}}\right) \tag{17.a}$$

$$\left|\psi_{\alpha\beta s}\right| = \sqrt{{\psi_{\alpha s}}^2 + {\psi_{\beta s}}^2} \tag{17.b}$$

The rotor instantaneous position is specified by θ_r. Hence, with a reference frame tied to the rotor, the relative position of the stator's magnetic field vector, known as the "slip angle," is described as $\theta_s - \theta_r$. Aligning the reference frame yields a simplified model as illustrated in (18):

$$v_{qs} = \omega_s \psi_{ds} = v_s \,; v_{ds} = 0 \tag{18}$$

The electromagnetic torque depends on the *iqr* current component and can be regulated through the *v′qr*. The *idr* current component can be regulated by the *v′dr* voltage component. The controller is shown in Fig. 2(b), where the measures coming from the stator current sensors, the stator voltage sensors, or the rotor current sensors may be susceptible to potential additive or multiplicative fault as it is represented in the figure (formulas available in section II.3). The errors between the actual rotor currents *idr* and *iqr* and their references are fed into PI controllers with the aim of producing the control voltages *v′dr* and *v′qr*. These voltages are then corrected with decoupling terms *v′dr_ref* and *v′qr_ref* to establish the final reference voltages described in (19) and (20) [43]:

$$v_{dr\_ref} = R_r i_{dr} + \sigma L_r \frac{di_{dr}}{dt} - \omega_{slip} \sigma L_r i_{qr} \tag{19}$$

$$v_{qr\_ref} = R_r i_{qr} + \sigma L_r \frac{di_{qr}}{dt} + \omega_{slip}\left(\frac{L_m}{L_s}\psi_{ds} + \sigma L_r i_{dr}\right) \tag{20}$$

where

$$\psi_{ds} = \psi_s = L_M I_{ms} \,; \psi_{dr} = {}^{L_M^2 I_{ms}}\!/_{L_s} + \sigma L_r i_{dr} \,; \psi_{qr} = \sigma L_r i_{qr} \,; \omega_{slip} = \omega_s - \omega_r \,; \sigma = 1 - {}^{L_M^2}\!/_{L_s L_r} \,.$$

Both rotor currents (i_{dr}, i_{qr}), in this control approach, must be regulated in accordance with their corresponding references, i_{dr_ref} and i_{qr_ref}. The generator's rotor is controlled by the PWM converter, which uses signals from the stator current and voltage, and the rotor current and position [37].

D. Fault Modeling

There are two main categories of faults: additive and multiplicative faults [44]. It is essential to compare between their effects with the

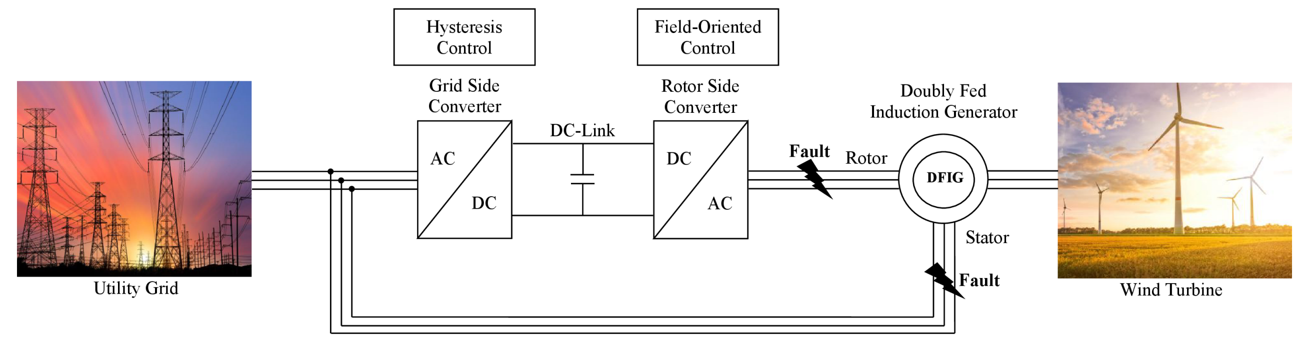

Fig. 1. Controlled grid-connected wind energy conversion system based on doubly fed induction generator scheme.

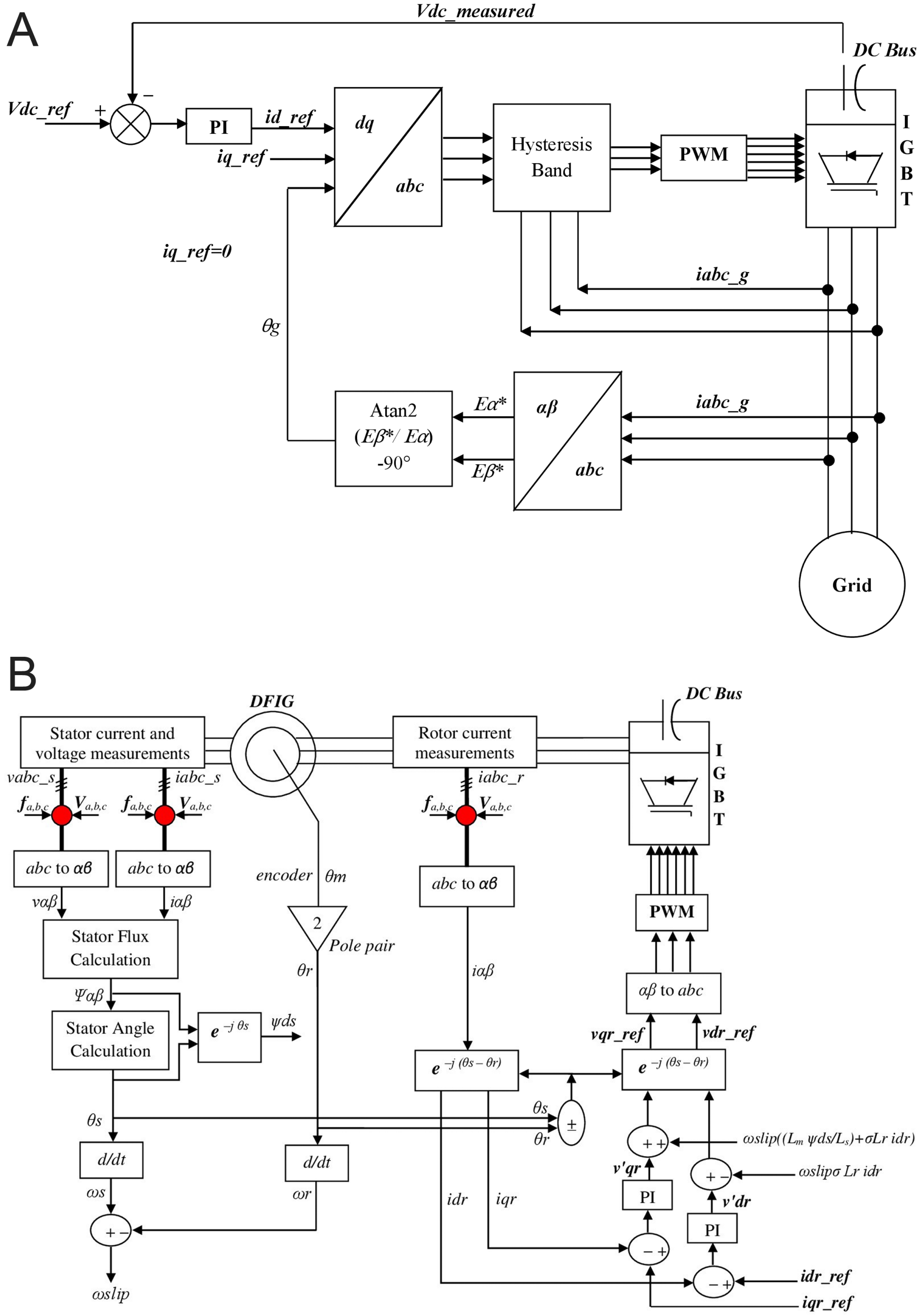

Fig. 2. Control schemes of the system: (a) Grid side converter, (b) Stator side converter.

aim of improving the functionality and the effectiveness of the control system and giving a FTC.

1) Additive Faults

Additive faults arise when biases and drifts accumulate in the measurements or when the characteristics of the noises in the sensor vary. Three-phase signals with additive faults are modeled in (21) [44]:

$$y^{m}_{abc}(k) = y_{abc}(k) + V(k) + f(k) \tag{21}$$

$$y^{m}_{abc}(k) = [\,y^{m}_{a}(k) + y^{m}_{b}(k) + y^{m}_{c}(k)]^{T},$$

and $y_{abc}(k) = \left[y_{a}(k) + y_{b}(k) + y_{c}(k)\right]^{T}$ are the measured and real three-phase signals, accordingly. *V*(*k*) is a zero-mean white noise

Gaussian sequence with covariance *RV*. $f(k)=[fa(k)fb(k)fc(k)]^T$ is the additive faults' vector, with $f(k) \neq 0$, for $i \in \{a,b,c\}$.

2) Multiplicative Faults
Changes in the gain of a sensor can be considered as multiplicative faults. In the presence of a multiplicative fault, measured signals $y^m_{abc}(k)$ and real signals $y_{abc}(k)$ are related by (22) [44]:

$$y^m_{abc}(k)=\varepsilon(k).y_{abc}(k)+V(k) \tag{22}$$

Where $\varepsilon(k)=\text{diag}\ \{\varepsilon a(k), \varepsilon b(k), \varepsilon c(k)\}$ is the sensors gains' matrix whith $\varepsilon i\ (k) \neq 1$.

III. RESULTS AND DISCUSSION

The WECS based on DFIG was tested in simulations under diverse sensor fault conditions occurring at different operating stages. The goal was to assess how the system responds to various fault types and intensities and to derive overall conclusions on its sensitivity to these faults. The results are expected to guide the design of a reliable FTC scheme.

The control schemes of the WECS based on DFIG, shown through Fig. 2, utilizes three primary input references: the DC-link voltage reference ***Vdc_ref***, the direct-axis rotor current reference ***idr_ref***, and the quadrature-axis rotor current reference ***iqr_ref***. The feedback loop is a critical part of the control system, as sensor faults can significantly influence control accuracy. The DC-link voltage (***Vdc***) is directly measured via a voltage sensor. However, the d-q rotor currents (***idr*** and ***iqr***) are derived from the measured three-phase currents and voltages of the stator along with the rotor currents. Therefore, in this study, the authors focus on three types of sensor faults in simulation: stator voltage sensor faults, stator current sensor faults, and rotor current sensor faults. Each simulation stage incorporates various paths to reflect multiple fault scenarios, including different symmetrical and asymmetrical fault magnitudes (e.g., ±5%, ±20%, −15%, +3%, +10%), different types (additive or multiplicative), and different affected phases. The theoretical outcomes and observations show that

- Faults in stator voltage, stator current, and rotor current sensors do not affect the regulation of the DC-link voltage. These are due to the fact that the DC-link voltage is regulated by the GSC using a control loop that is independent of the RSC loop. The GSC maintains using a PI controller as illustrated in (23) and (24) below

$$e_{dc}(t)=V_{dc\_ref}(t)-V_{dc}(t) \tag{23}$$

$$U_{GSC}(t)=k_p e_{dc}(t)+k_i \int e_{dc}(t)dt \tag{24}$$

This loop depends only on the measured DC-link voltage and does not depend on stator voltage/current or rotor current sensors. This observation is consistent with the system's decoupled control structure: the two controllers RSC and GSC are independent.

- Stator voltage and stator current faults do not have a direct impact on the direct-quadrature rotor current. However, rotor current faults alter the direct-quadrature rotor current.

  Explanation: Although the RSC regulates the direct-quadrature rotor currents based on feedback from stator voltage/current and rotor current measurements, their values do not directly depend on stator voltage or stator current sensors. This is due to the fact that the direct-quadrature rotor currents are related to stator angle θ_s, rotor angle θ_r, and the $\alpha\beta$ rotor current components obtained from Park and Clarke transformations applied to $i_r(abc)$ illustrated before in Fig. 2(b). So stator faults do not directly influence the d-q rotor current components.

- Additive and multiplicative faults of equivalent magnitude yield nearly identical effects: an additive fault of $+a\%$ has a similar effect as a multiplicative gain of $(1+a\%)$.

  Explanation: Let the true measurement be x. Then the additive fault is $+a\%$, and the multiplicative fault is $(1+a\%)$.

In both cases, the controller receives the same faulty signal formulated through (25):

$$x_{faulty}=x+x.a\%=x.(1+a\%) \tag{25}$$

Hence, for small to moderate fault levels (linear range), additive and multiplicative faults produce equivalent effects.

- Faults distributed across phases are equivalent to a single-phase fault of combined magnitude. Applying faults separately to the first, the second, and the third phase of a sensor, with magnitudes of $a\%$, $b\%$, and $c\%$, results in the same effect as applying a total fault of $(a\%+b\%+c\%)$ to a single phase.

  Explanation: The transformation from three-phase to direct-quadrature components is linear. The transformation can be modeled in (26):

$$\begin{bmatrix} i_d \\ i_q \end{bmatrix}=f\begin{bmatrix} i_a \\ i_b \\ i_c \end{bmatrix} \tag{26}$$

If each is affected by an additive fault $\Delta a, \Delta b, \Delta c$ respectively, the transformation becomes as illustrated in (27) below:

$$\begin{bmatrix} i_d \\ i_q \end{bmatrix}_{faulty}=f\begin{bmatrix} i_a+\Delta a \\ i_b+\Delta b \\ i_c+\Delta c \end{bmatrix}=f\begin{bmatrix} i_a \\ i_b \\ i_c \end{bmatrix}+f\begin{bmatrix} \Delta a \\ \Delta b \\ \Delta c \end{bmatrix} \tag{27}$$

The change in dq currents is a linear combination of the individual phase faults. Therefore, the total effect on the system is approximately equal to that caused by applying the sum of the phase faults to a single phase, as described in (28):

$$Equivalent\,Fault=\Delta a+\Delta b+\Delta c \tag{28}$$

This result holds under the assumption of linearity and balanced operation.

A. Effect of Stator Voltage Sensor Faults
The first stage of analysis is based on the injection of varying symmetrical and asymmetrical amplitudes of additive and multiplicative faults to the stator voltage sensor. Faults are injected into the first phase of the stator voltage, and the obtained results, from Fig. 3 to Fig. 10, are analyzed and discussed. Similar trends are observed when faults are distributed among all three stator voltage phases. The amplitudes of faults are detailed in Fig. 3; further amplitudes are shown in Table I.

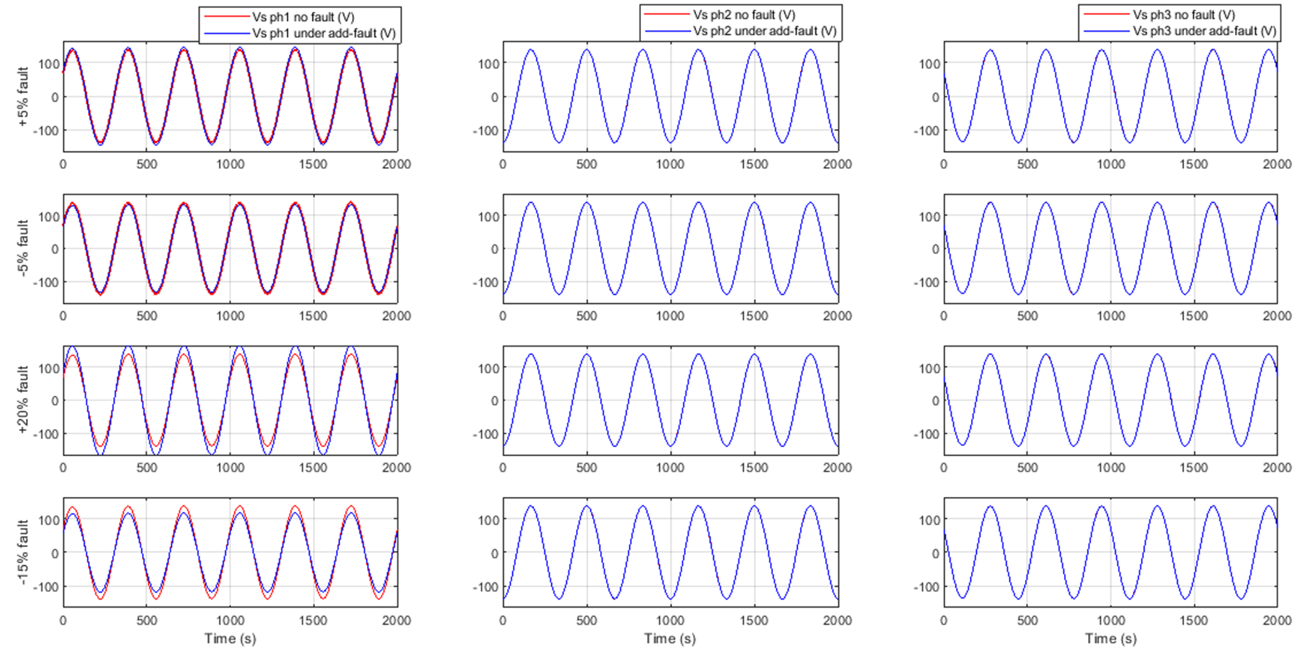

Fig. 3. Faults applied to the first-phase stator voltage sensor.

TABLE I. STATISTICS OF KEY ELECTRICAL PARAMETERS UNDER STATOR VOLTAGE SENSORS FAULTS

Electrical Parameters	No Fault	−20%	−15%	−5%	+3%	+5%	+10%	+20%
Stator Voltage (V) (Faulty)	±138.5	±110.8	±117.75	±131.57	±142.65	±145.42	±152.35	±166.2
Stator Active Power (VA)	101	95	97.5	100.5	101.5	102.8	103.5	104.5
Stator Reactive Power (VAR)	1150	1075	1095	1125	1160	1175	1190	1225
Grid Active Power (VA)	−103.85	−103.9	−104.05	−104.20	−103.45	−103.55	−103.72	−103.80
Grid Reactive Power (VAR)	−396	−399.5	−398.5	−397	−395.5	−395.3	−395	−394
Rotor Active Power (VA)	−150.45	−150.50	−150.48	−150.46	−150.43	−150.40	−150.35	−150.33

1) Stator Current, Active Power, and Reactive Power

Additive and multiplicative faults that originate in stator voltage sensor produce a perturbation in the stator current; fluctuating within the range of approximately ±5*A*, hence a perturbation of about 50% of the stator current that ranges between ±10*A*. Fig. 4 illustrates the response of the first-phase stator current under these conditions.

The impact of stator voltage sensor faults on stator active power is minimal. However, the reactive power is significantly affected. The stator active and reactive powers are given in (9.a) and (9.b), and they are directly related to both stator voltage and current. Any deviations in their values lead to an overestimation of the active/reactive power. Responses of active and reactive powers of the stator are shown in Fig. 5.

These results confirm that the reactive power varies approximately linearly with the applied fault magnitude: positive additive/multiplicative faults increment the reactive power's amount, and the higher is the fault, the higher is the augmentation. Conversely, negative additive/multiplicative faults decrement the amount of the reactive power, and the higher is the fault, the lower is the reduction. Further results are summarized in Table I.

2) Grid Current , Active Power, and Reactive Powers

The grid current, which fluctuates between ±2.5*A*, experiences a perturbation within the narrow range of ±1.5*A* when stator voltage sensor faults are applied, as depicted in Fig. 6. In contradiction to the grid current behavior, the grid voltage remains practically unaffected and does not significantly change.

Furthermore, the grid active and reactive powers are only slightly influenced, with negligible dependency on the fault magnitude, as seen in Fig. 7, indicating the robustness of the grid-side operation under stator voltage sensor faults.

3) Rotor Voltage, Current, Active, and Reactive Power

Figs. 8 and 9 reveal that the rotor current is marginally influenced by stator voltage sensor faults. However, the rotor voltage experiences significant waveform distortion. This is expected due to the interdependence between the stator and rotor circuits via the magnetic coupling in the DFIG.

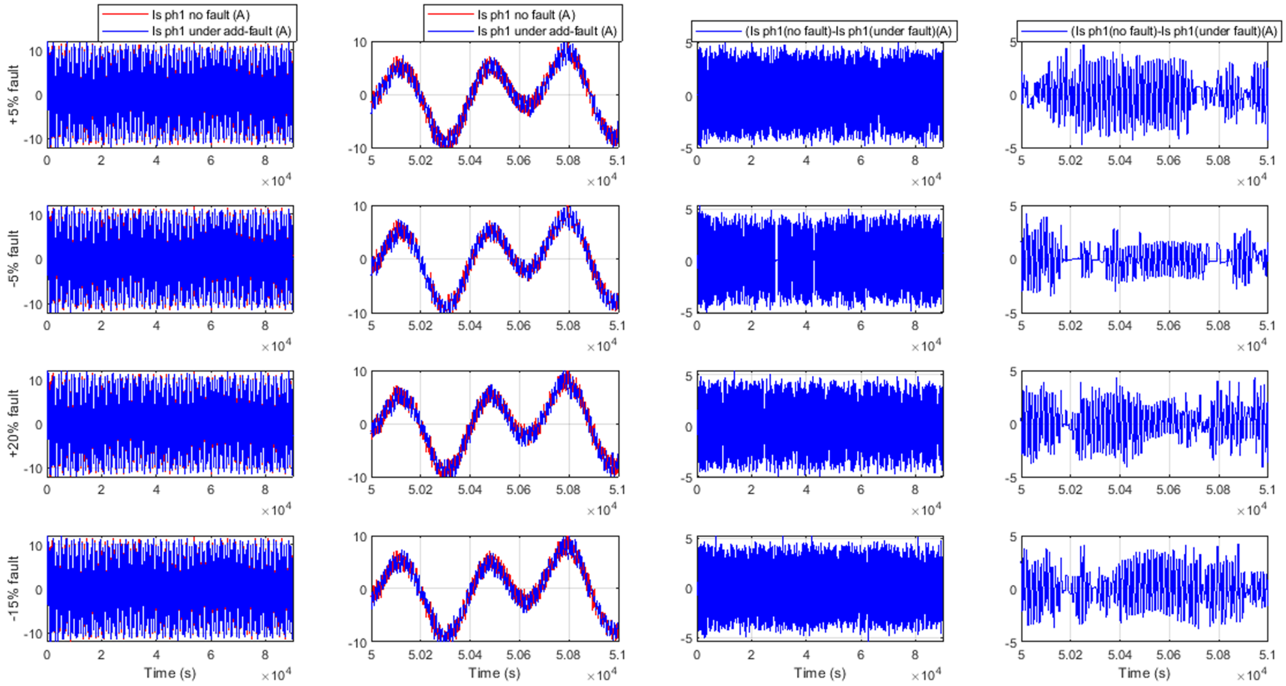

Fig. 4. First-phase stator current response and its corresponding error under stator voltage sensor faults.

The rotor active power, expressed by (10.a), is slightly perturbed due to current and voltage perturbations. However, the rotor reactive power, given by (10.b), is heavily distorted under fault conditions. This indicates that faults in the stator voltage measurement propagate significantly to the rotor's parameters behavior, causing complete degradation of their waveform quality. The behavior of active and reactive powers of the rotor is shown in Fig. 10. Further results are summarized in Table I.

B. Effect of Stator Current Sensor Faults

This section analyzes the impact of varying symmetrical and asymmetrical amplitudes of stator current sensor faults on the system performance. The assessment focuses on how these faults influence electrical variables such as stator and grid current, rotor voltage, and the corresponding active and reactive powers. The simulation results presented in Figs. 11–17 correspond to multiple amplitudes of faults applied to the first phase of the stator current sensor. Similar trends

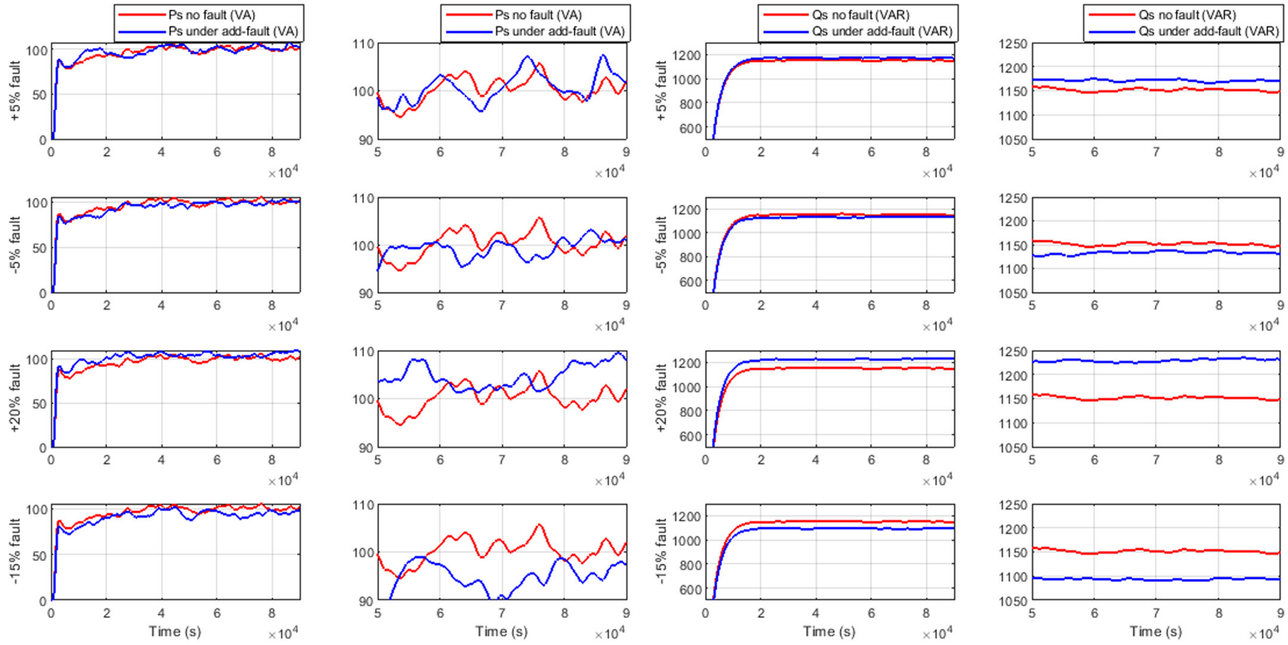

Fig. 5. Stator active and reactive powers responses under stator voltage sensor faults.

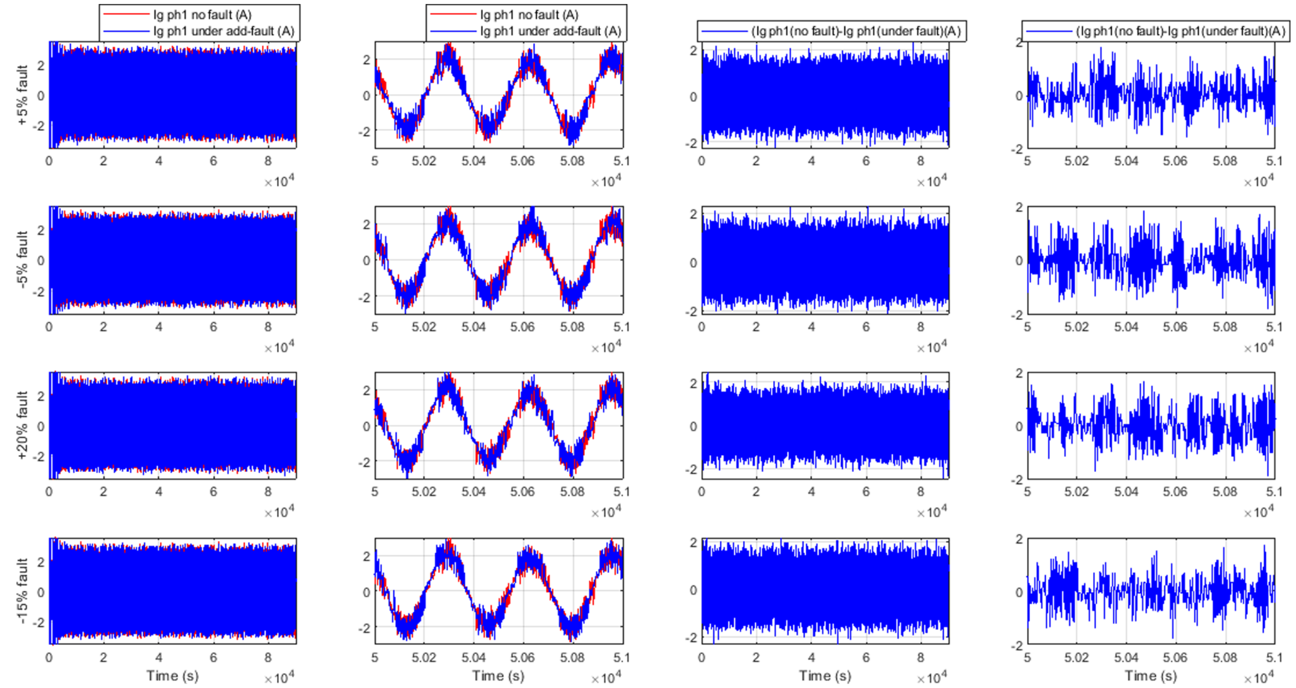

Fig. 6. First-phase grid current response and its corresponding error under stator voltage sensor faults.

are observed when faults are distributed among all three stator current phases. The amplitudes of faults are detailed in Fig. 11; further amplitudes are shown in Table II.

1) Stator Current, Active Power, and Reactive Power

Fig. 11 illustrates the behavior of the three-phase stator current under different fault scenarios: (a) fault applied to phase a only, (b) faults applied to phases a and b, and (c) faults applied to all three phases. The figures reveal that faults affecting only one or two phases also perturb the remaining healthy phases due to the intrinsic coupling of the three-phase system. This interference propagates through the control system, altering the current regulation.

Fig. 12 presents the impact on stator active and reactive power. Observations from Fig. 12 indicate that stator active power remains nearly constant regardless of the fault magnitude, indicating

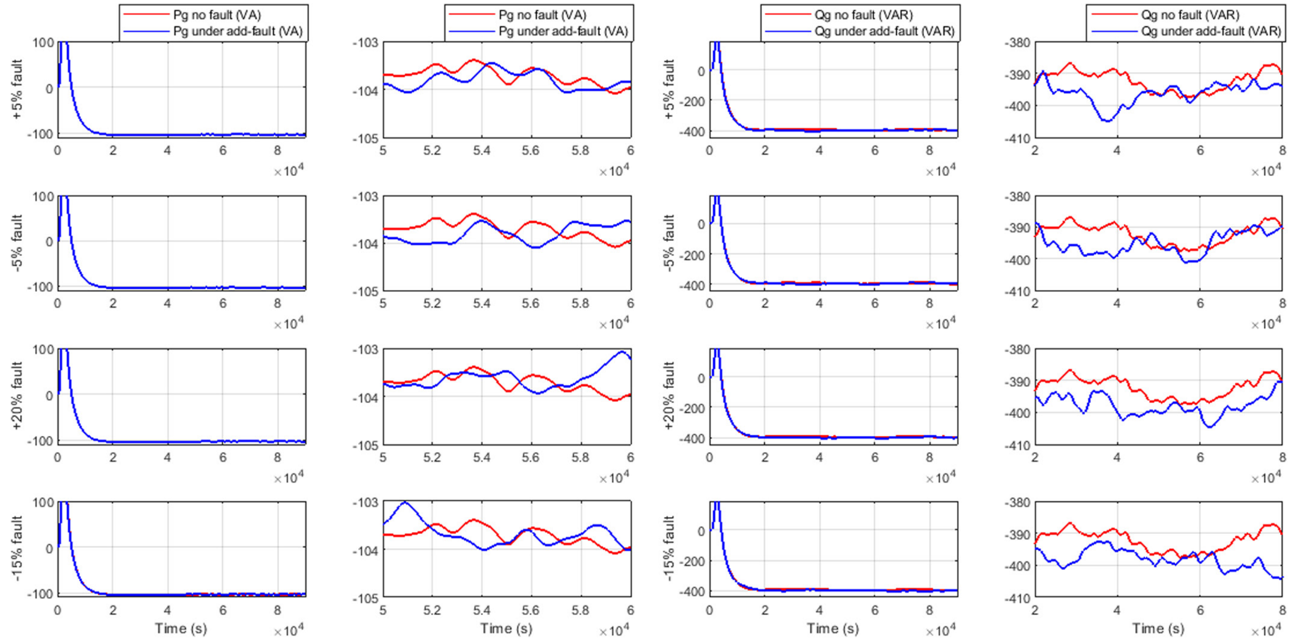

Fig. 7. Grid active and reactive powers responses under stator voltage sensor faults.

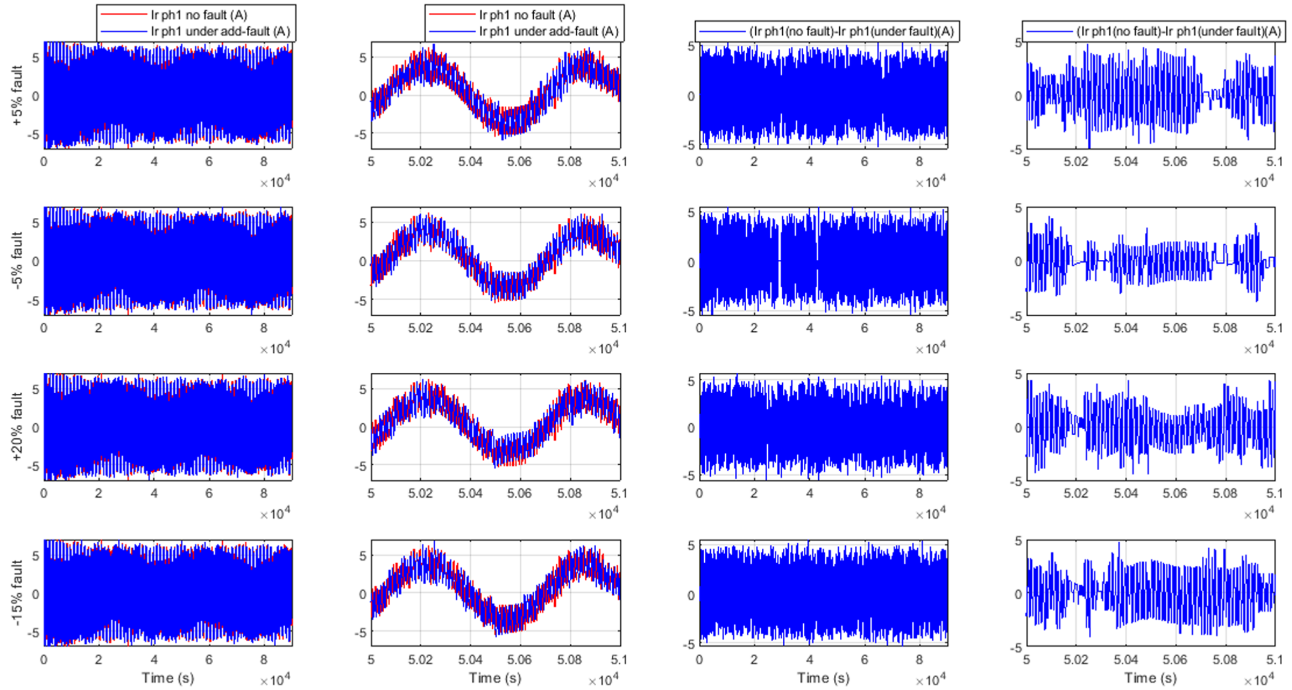

Fig. 8. First-phase rotor current response and its corresponding error under stator voltage sensor faults.

robustness to sensor faults. However, stator reactive power shows a proportional response to the fault magnitude: a positive additive fault (e.g., +5%, +20%) increases the measured reactive power, while a negative additive fault (e.g., −5%, −20%) decreases it. This variation aligns with the gain behavior of additive faults; the higher is the gain, the higher is the variation. Further results are summarized in Table II.

2) Grid Current, Active Power, and Reactive Power

Fig. 13 displays the first-phase grid current response and its deviation under varying stator current sensor faults. The grid current is only marginally affected, with fluctuations limited to ±2*A*. This is expected, as the stator fault impacts are partially decoupled from the grid via the back-to-back converter.

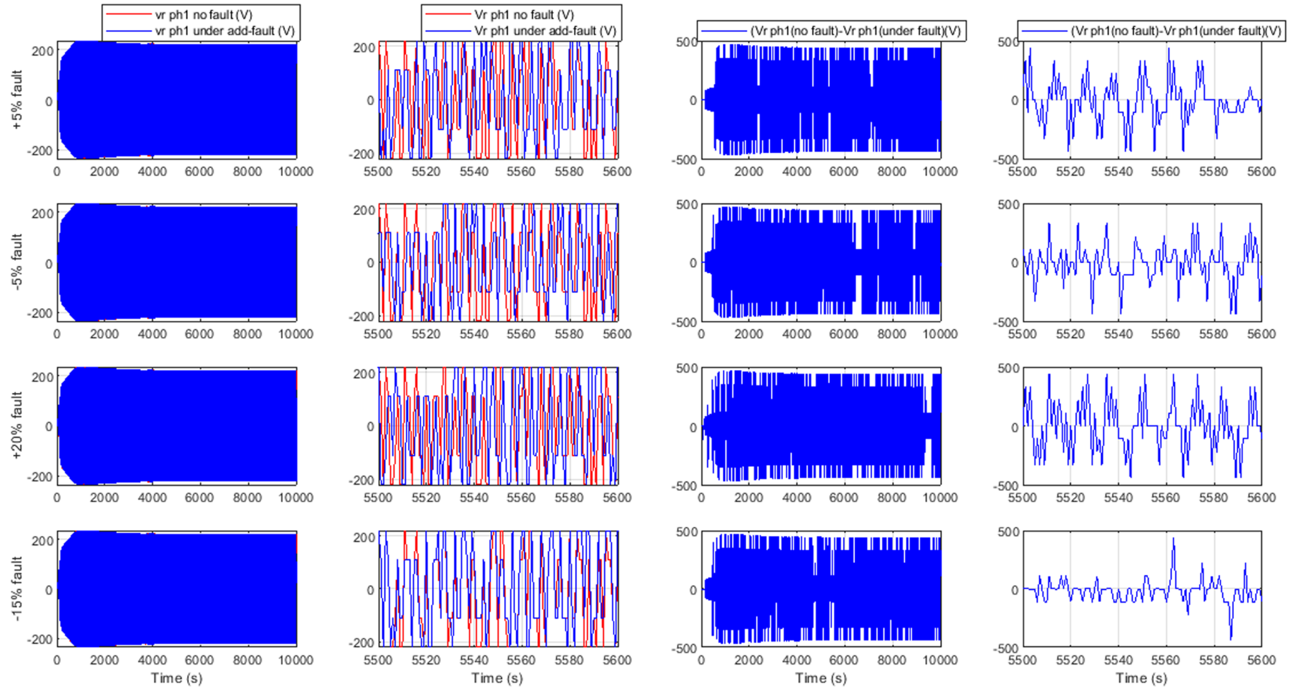

Fig. 9. First-phase rotor voltage response and its corresponding Error under stator voltage sensor faults.

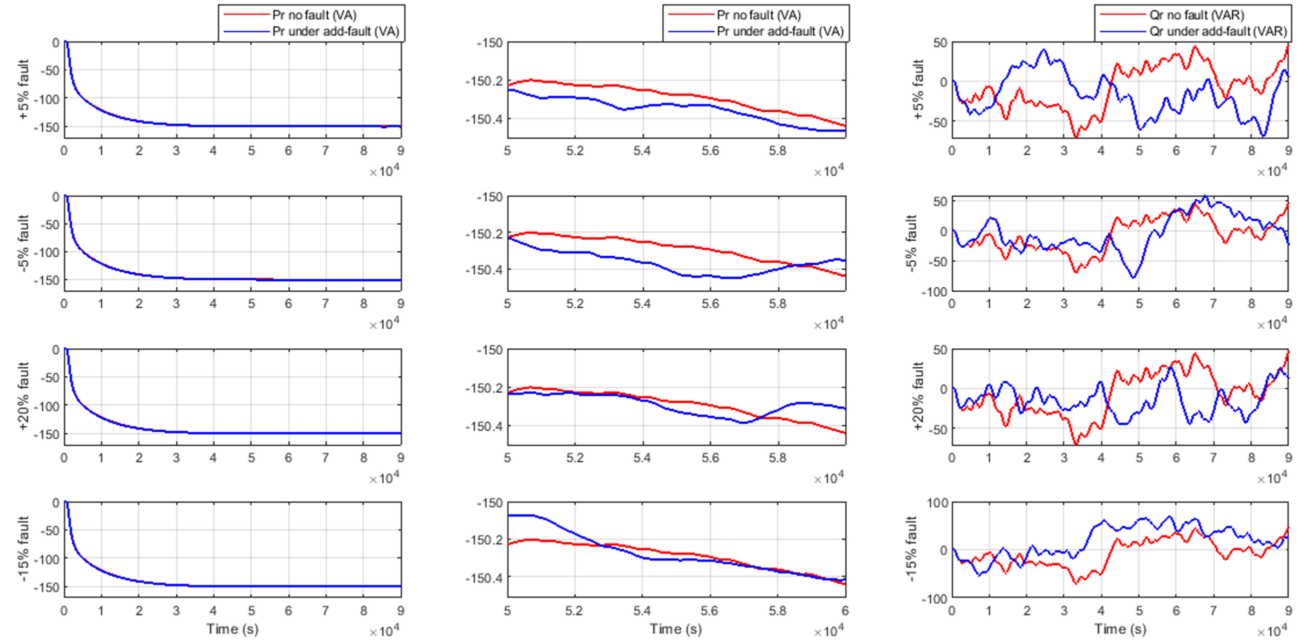

Fig. 10. Rotor active and reactive powers responses under stator voltage sensor faults.

The corresponding active and reactive powers, illustrated in Fig. 14, are computed similarly to (14.a) and (14.b). The plots show negligible deviations, regardless of the fault magnitude, confirming that stator current sensor faults have limited impact on the grid-side power flow.

3) Rotor Voltage, Current, Active, and Reactive Power

Fig. 15 presents the rotor current under faulted stator current sensor conditions. The observed perturbations are minor, bounded within ±5*A*. This is due to the indirect effect of stator measurements on rotor current control through the FOC strategy.

Fig. 16 highlights the impact on rotor voltage. Here, the faults significantly distort the rotor voltage waveform, with observable nonlinear deviations in both amplitude and waveform shape. This is attributed to the distorted stator current reference used in the control algorithm.

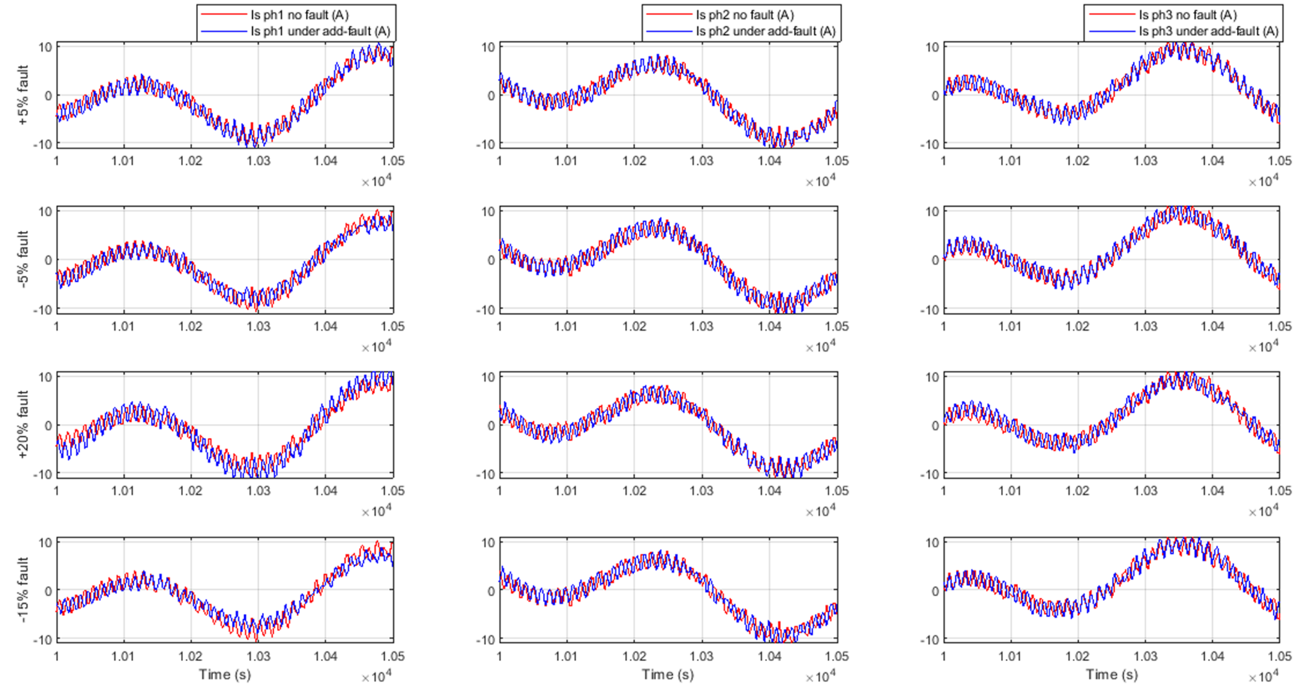

Fig. 11. Faults applied to the first phase of stator current sensor.

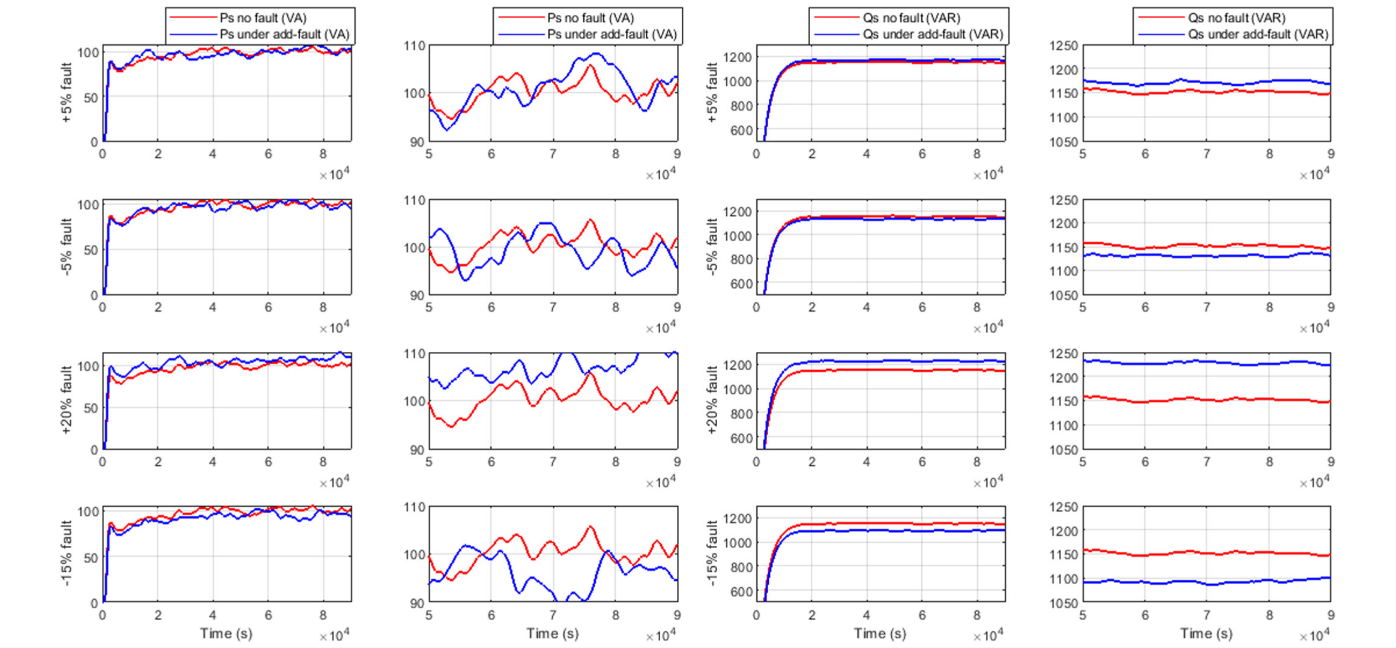

Fig. 12. Stator active and reactive powers responses under stator current sensor faults.

Fig. 17 shows that Rotor active power remains relatively stable, indicating that torque production is largely unaffected. However, rotor reactive power is substantially distorted. Its waveform is visibly destroyed under fault conditions, indicating strong sensitivity to stator current sensor faults. This can be analytically justified since the reactive power (10.b) depends heavily on the quadrature current component, which is directly influenced by stator current feedback. Inaccurate measurements lead to improper control of rotor current references, thereby distorting.

C. Effect of Rotor Current Sensor Faults

This section analyzes the impact of varying symmetrical and asymmetrical amplitudes of rotor current sensor faults on the WECS based on DFIG performance. The faults are applied to the first

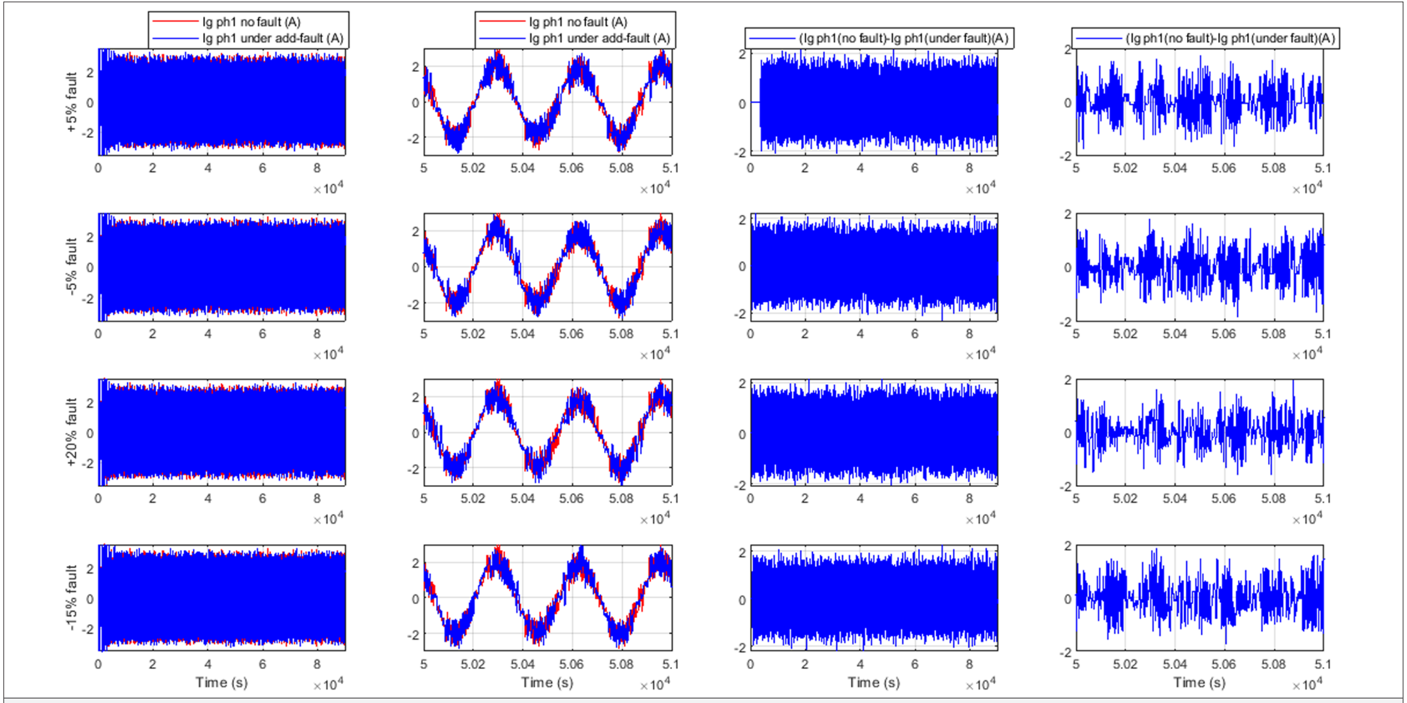

Fig. 13. First-phase grid current response and its corresponding error under stator current sensor faults.

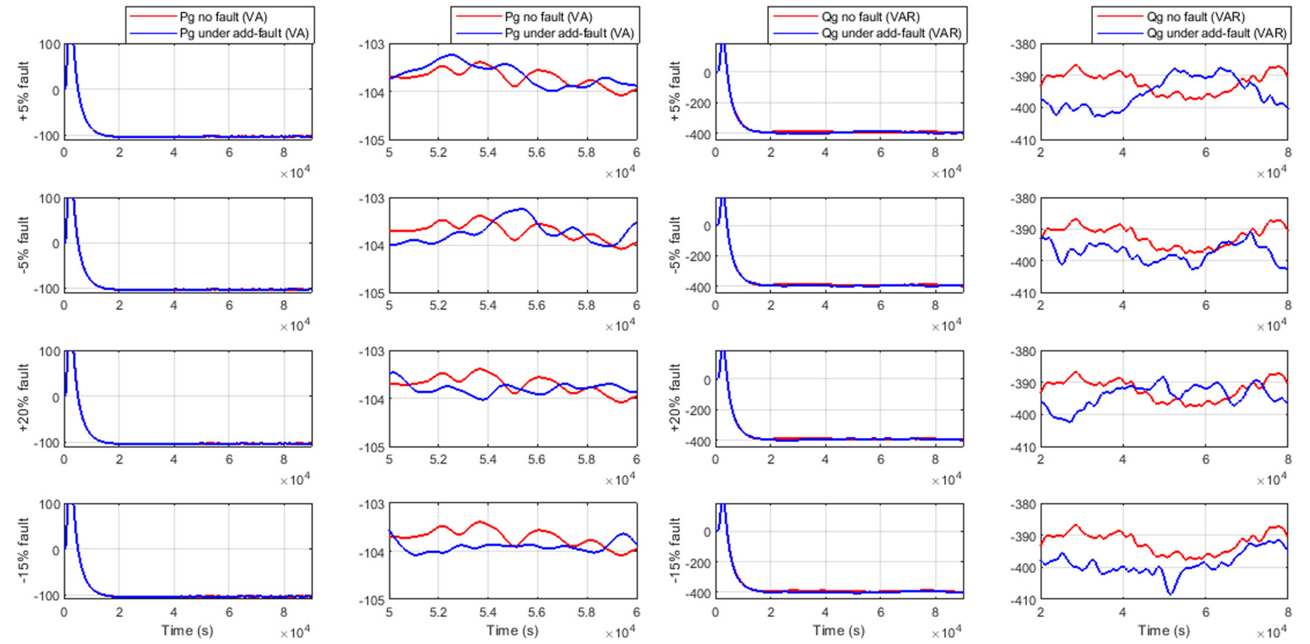

Fig. 14. Grid active and reactive powers responses under stator current sensor faults.

rotor current phase sensor, and the system response is observed through Figs. 18–25. The fault magnitudes considered include −15%, +3%, +10%, ±5%, ±20%, and ±50%. All results are summarized in Table III.

1) Direct-Quadrature Rotor Current Response

Consider the reference values of the direct and quadrature rotor currents as $i_{rd\_ref}=1A$ and $i_{rd\_ref}=3.5A$, respectively. When the rotor current sensor experiences an additive or a multiplicative fault, the faulty measurements are fed back and processed by the control loop as if they were accurate. Consequently, the controller acts to minimize the error between the faulty measurements and their references, leading to biased control actions.

- Considering positive faults, the measured currents appear artificially higher than their actual values. The controller then reduces the control effort, resulting in actual rotor currents i_{rd} and i_{rq} that fall below their references.

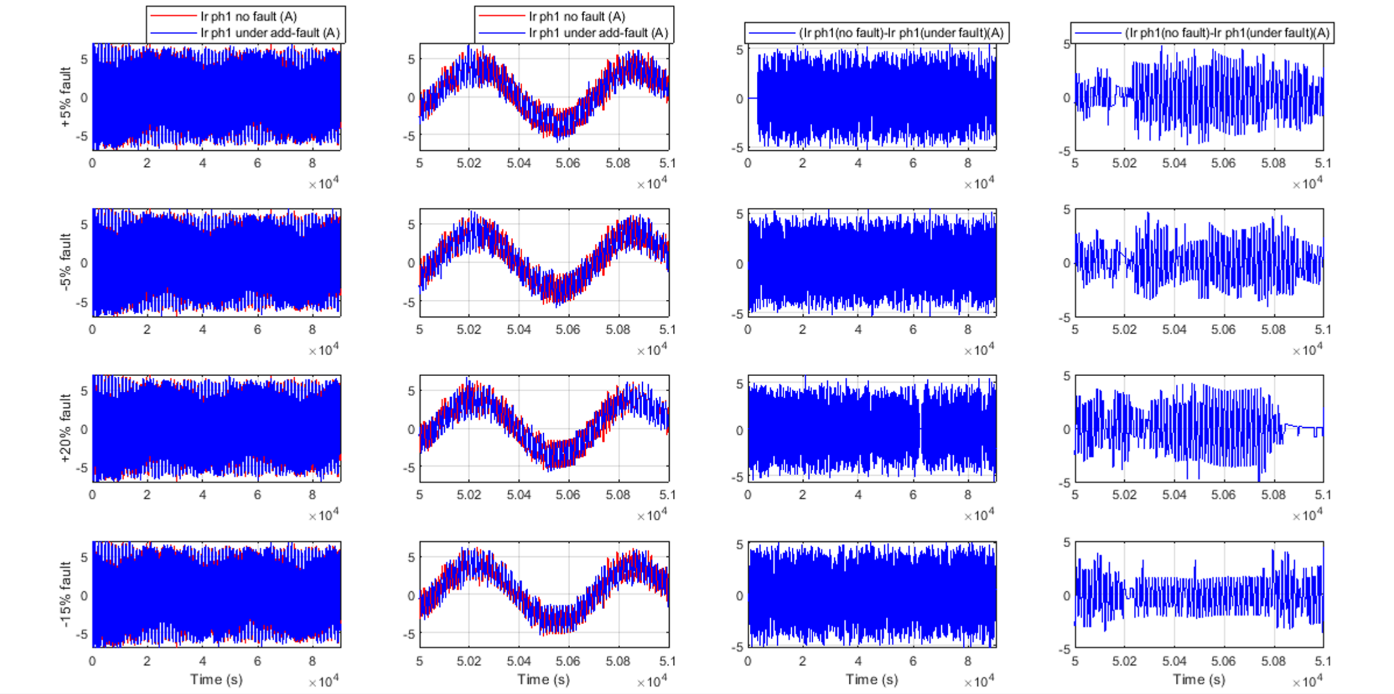

Fig. 15. First-phase rotor current response and its corresponding error under stator current sensor faults.

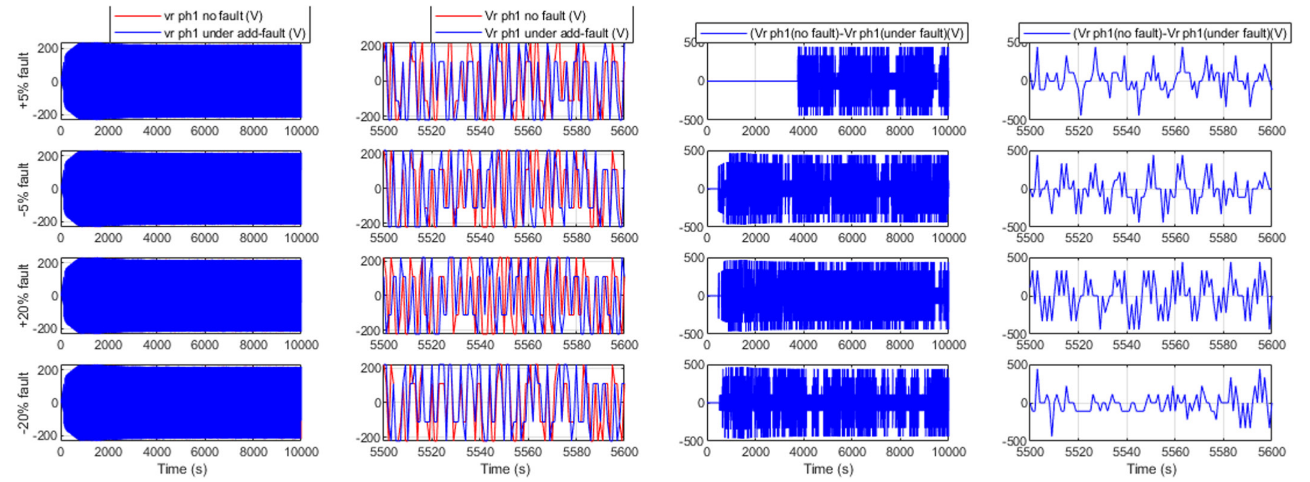

Fig. 16. First-phase rotor voltage response and its corresponding error under stator current sensor faults.

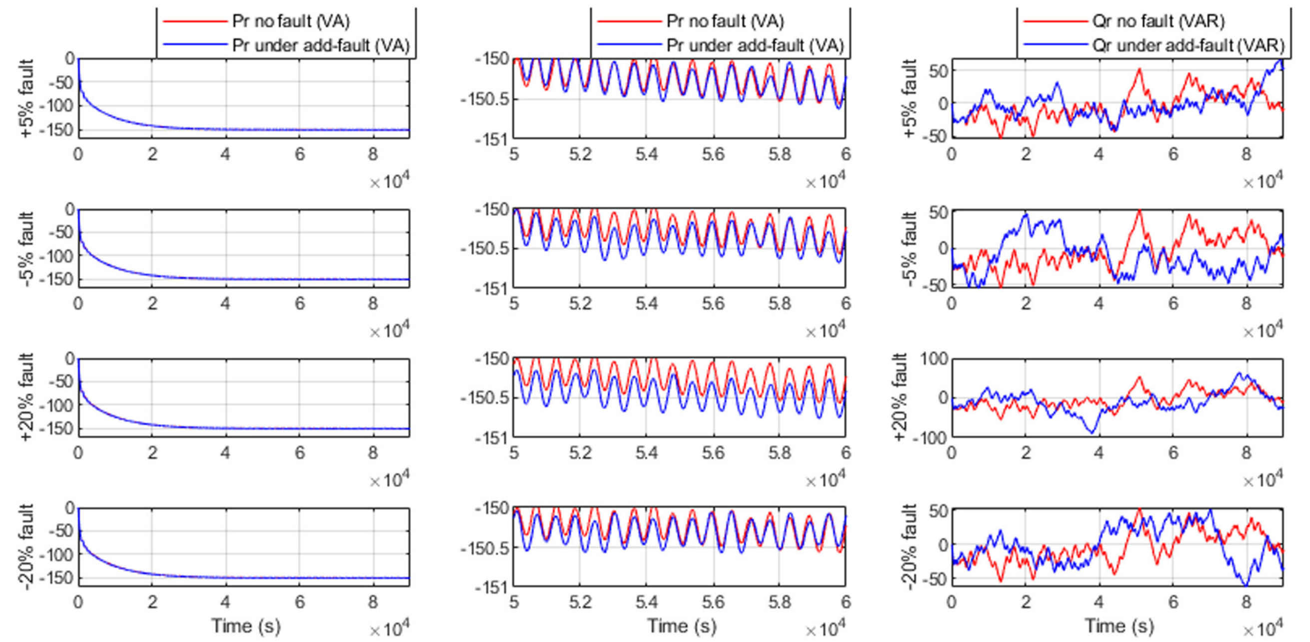

Fig. 17. Rotor active and reactive powers responses under stator current sensor faults.

TABLE II. STATISTICS OF KEY ELECTRICAL PARAMETERS UNDER STATOR CURRENT SENSORS FAULTS

Electrical parameters	No fault	−20%	−15%	−5%	+3%	+5%	+10%	+20%
Stator Active Power (VA)	101	95	97.5	100.5	101.5	102	105	107
Stator Reactive Power (VAR)	1150	1100	1110	1130	1160	1175	1190	1225
Grid Active Power (VA)	−103.85	−104	−103.95	−103.9	−103.45	−103.55	−103.72	−103.80
Grid Reactive Power (VAR)	−396	−400	−398.5	−397	−395.5	−395.3	−395	−393
Rotor Active Power (VA)	−150.45	−150.50	−150.48	−150.46	−150.43	−150.40	−150.35	−150.33

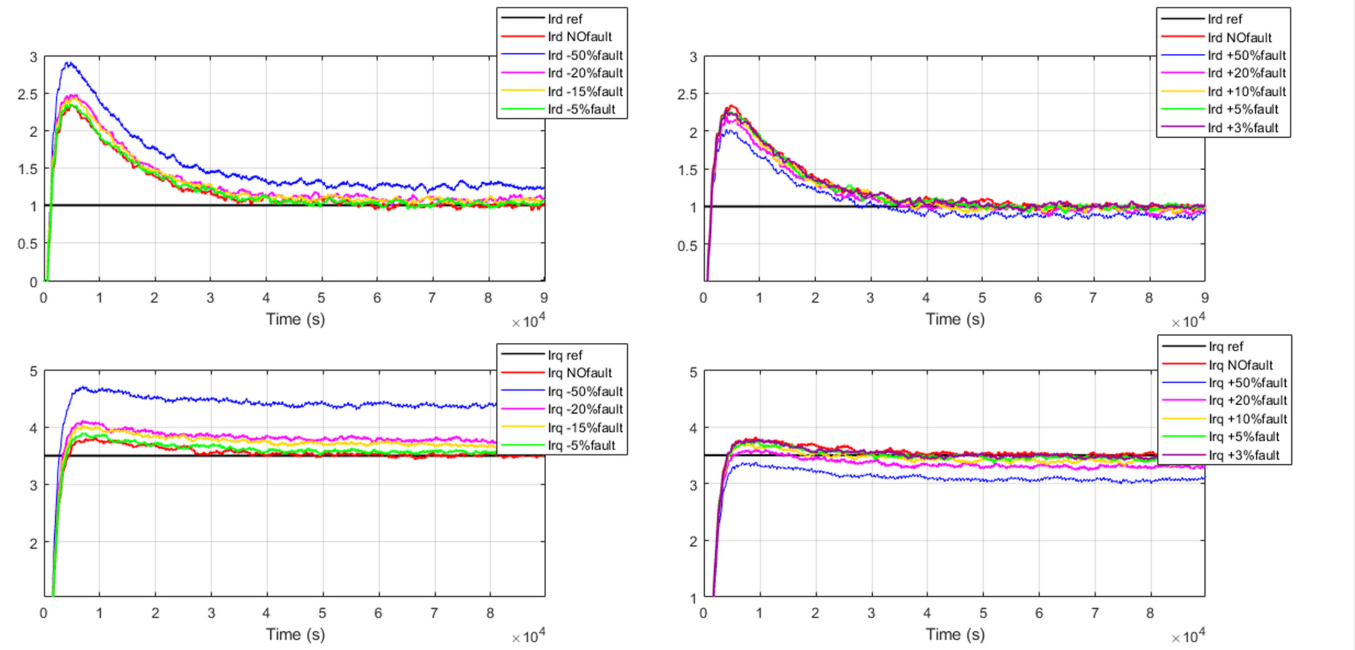

Fig. 18. Direct and quadrature rotor currents regulation under rotor current sensor faults.

- Conversely, for negative faults, the measured currents are perceived as lower than their actual values. The controller compensates by increasing the control effort, thereby pushing i_{rd} and i_{rq} above their references.

This behavior highlights the inverse relationship between the fault magnitude and the actual rotor current response, driven by the controller's attempt to regulate based on faulty feedback. Fig. 18 illustrates the direct-quadrature rotor current regulation under rotor current sensor faults.

It is evident from simulation results that negative faults (underreporting) lead to larger deviations from the references than positive ones. However, for small fault magnitudes (e.g., +3%, ±5%), the system response remains relatively close to the reference values.

2) Stator Current, Active Power, and Reactive Power

Rotor current sensor faults significantly affect the stator current, resulting in deviations in all the three phases. The stator current error ranges approximately within ±5*A* for a response that fluctuates between ±10*A*. These results are shown in Fig. 19.

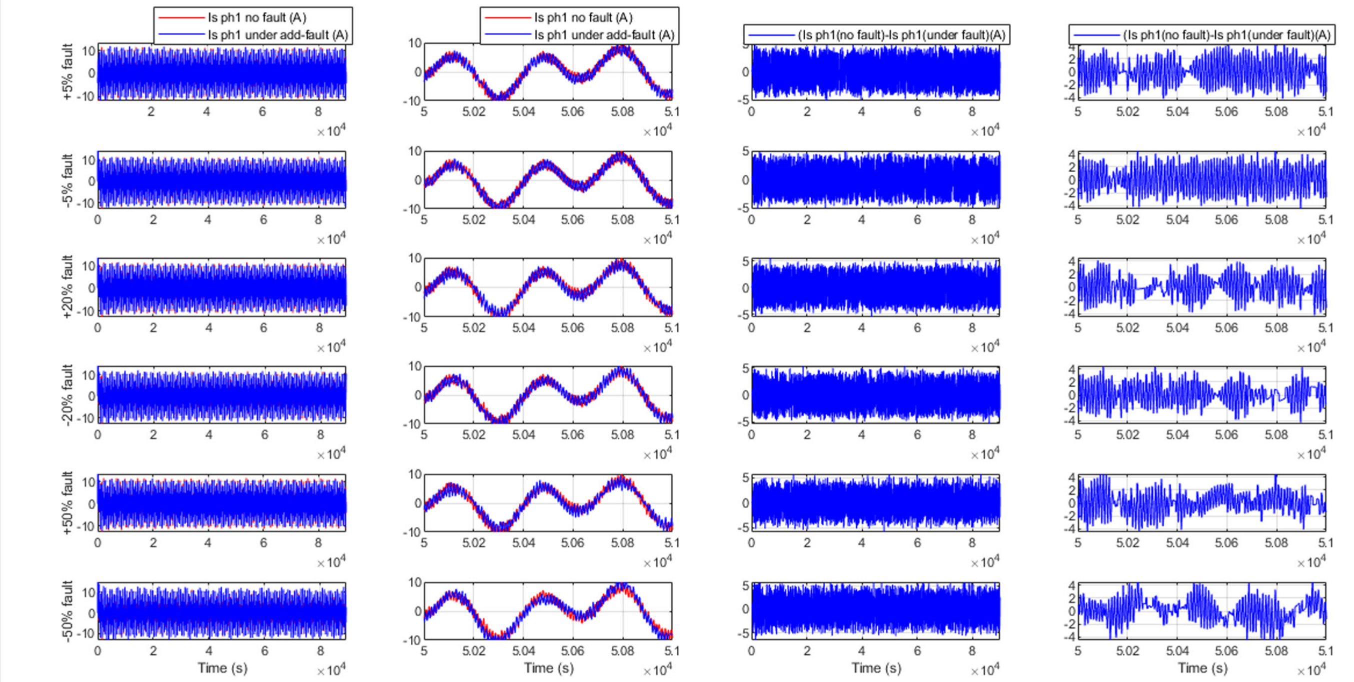

Fig. 19. First-phase stator current response and its corresponding error under rotor current sensor faults.

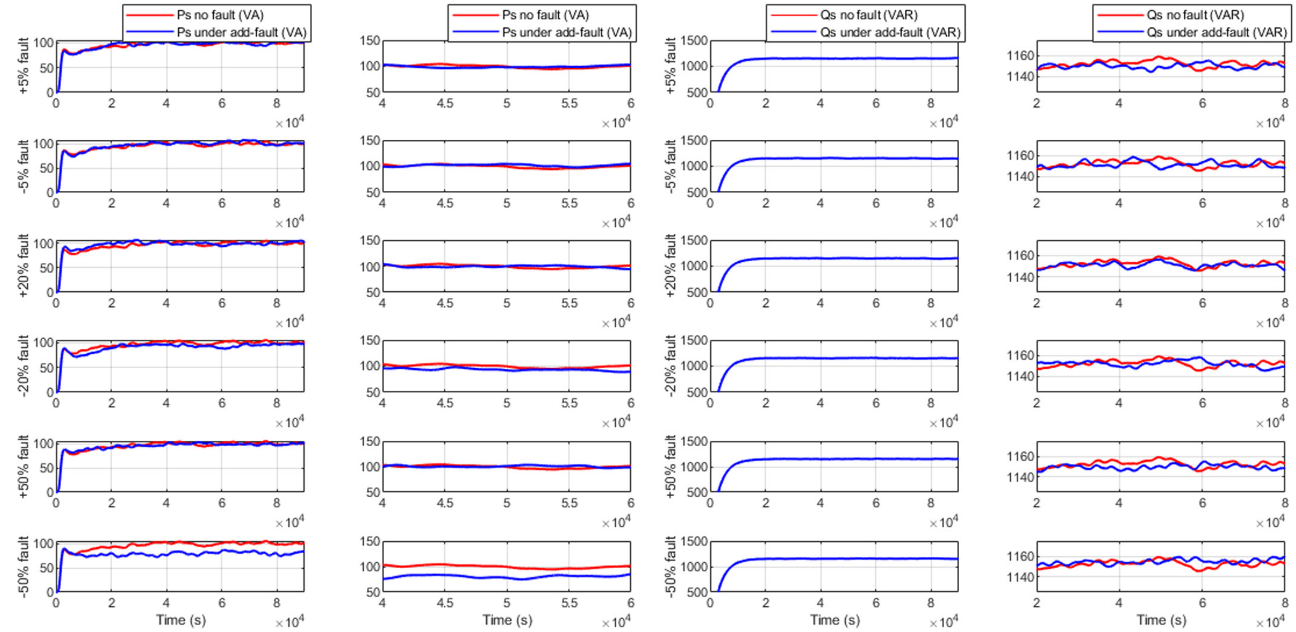

Fig. 20. Stator active and reactive powers responses under rotor current sensor faults.

Despite this, stator active power and reactive power are slightly influenced under larger fault conditions while remaining approximately stable under moderate faults, as shown in Fig. 20. This suggests that the control system can compensate for small faults but degrades under larger deviations.

3) Grid Current, Active Power, and Reactive Power

The grid current response and its deviation under varying rotor current sensor faults are shown in Fig. 21. The grid current is only marginally affected, with fluctuations limited to ±2*A*. This is expected, as the rotor fault impacts are partially decoupled from the grid via the back-to-back converter.

Regarding the grid active and reactive powers, Fig. 22 shows the following:

- Reactive power remains nearly unaffected under rotor current faults.
- Active power is directly correlated with the rotor current fault magnitudes: positive faults reduce the grid's active power, while negative faults increase it.

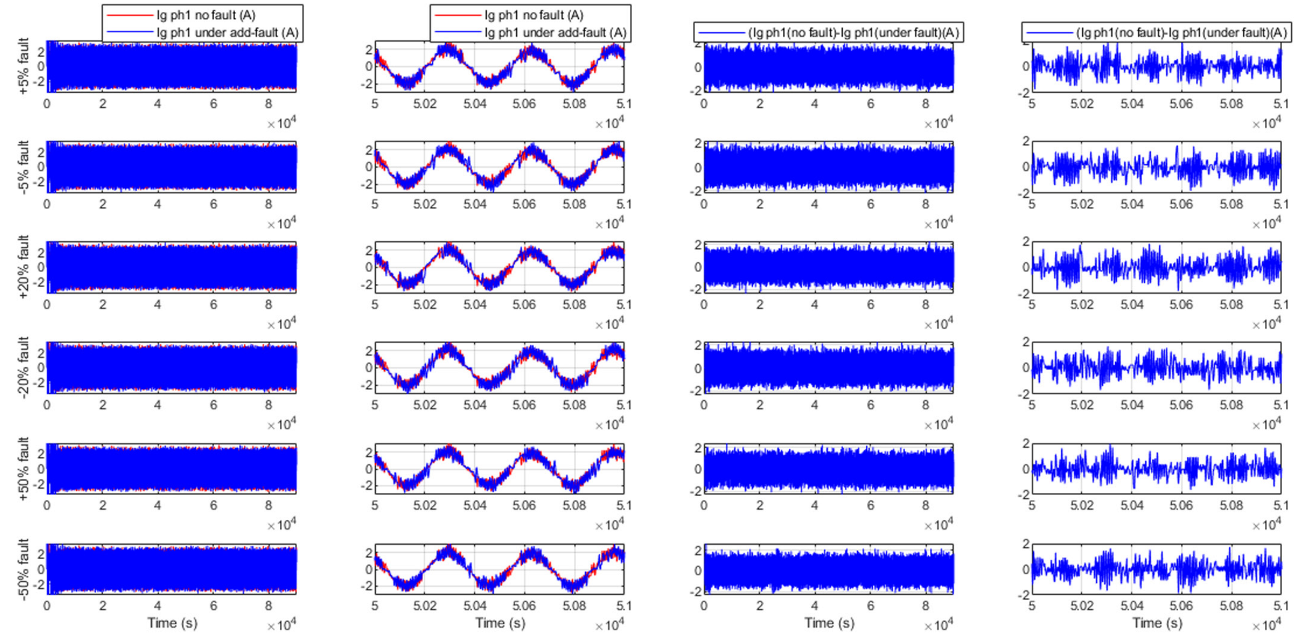

Fig. 21. First- phase grid current response and the corresponding error under different values of rotor current sensor' faults.

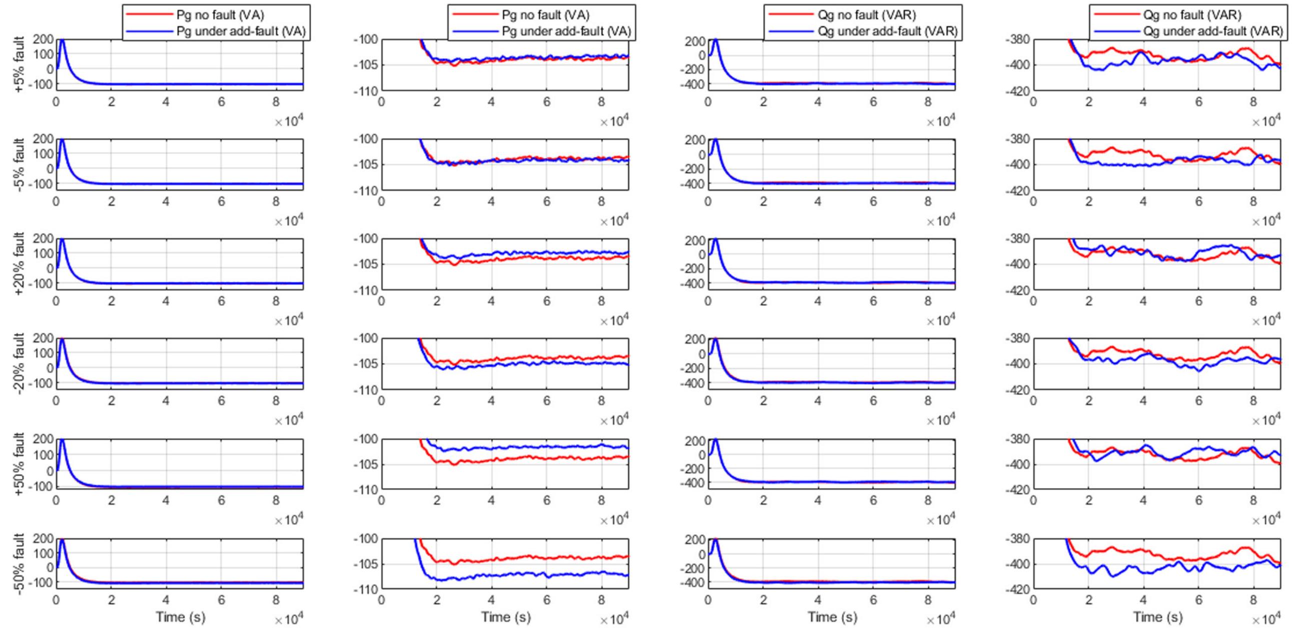

Fig. 22. Grid active and reactive power response under rotor current sensor faults.

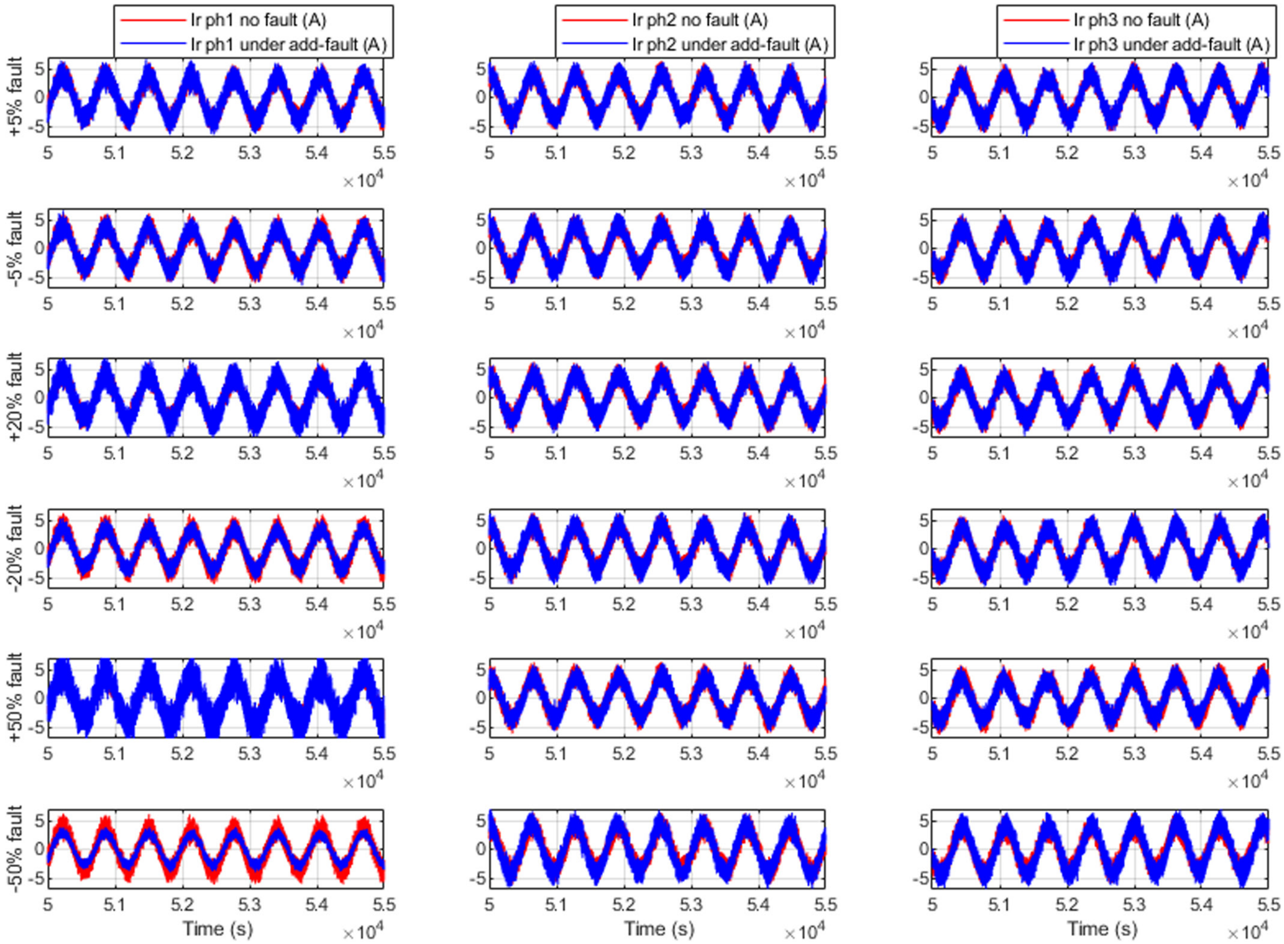

Fig. 23. Additive faults applied to the first phase of rotor current sensor.

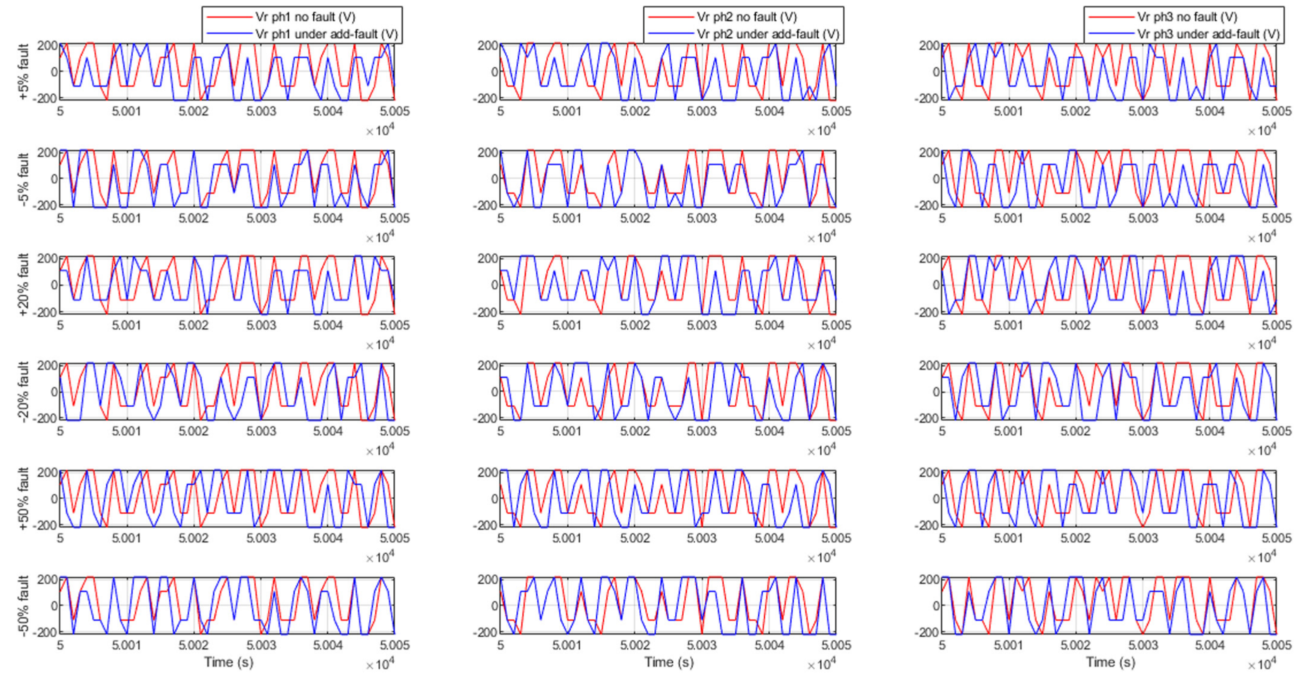

Fig. 24. Rotor first, second, and third voltage phases under rotor current sensor faults.

4) Rotor Current, Voltage, Active, and Reactive Powers

Rotor current faults not only impact the faulty phase but also propagate disturbance to the healthy phases. Fig. 23 illustrates that a single-phase fault significantly perturbs the other two rotor current phases, indicating inter-phase coupling within the DFIG system.

Furthermore, rotor voltage responses (Fig. 24) show complete distortion across all phases, even when the fault is isolated to one or two phases, revealing the vulnerability of rotor voltage control under sensor faults.

For the rotor active power, the fault impact is proportional to the fault magnitude: positive faults increase the magnitude of active power, while negative faults reduce it. Interestingly, the impact on rotor's active power is consistent across phases, implying a global effect of faults regardless of which rotor phase is affected. The obtained results concerning the rotor active power under rotor current sensor fault are shown in Fig. 25.

However, the rotor reactive power behaves unpredictably under fault conditions. As shown in Fig. 25, it is significantly disturbed and

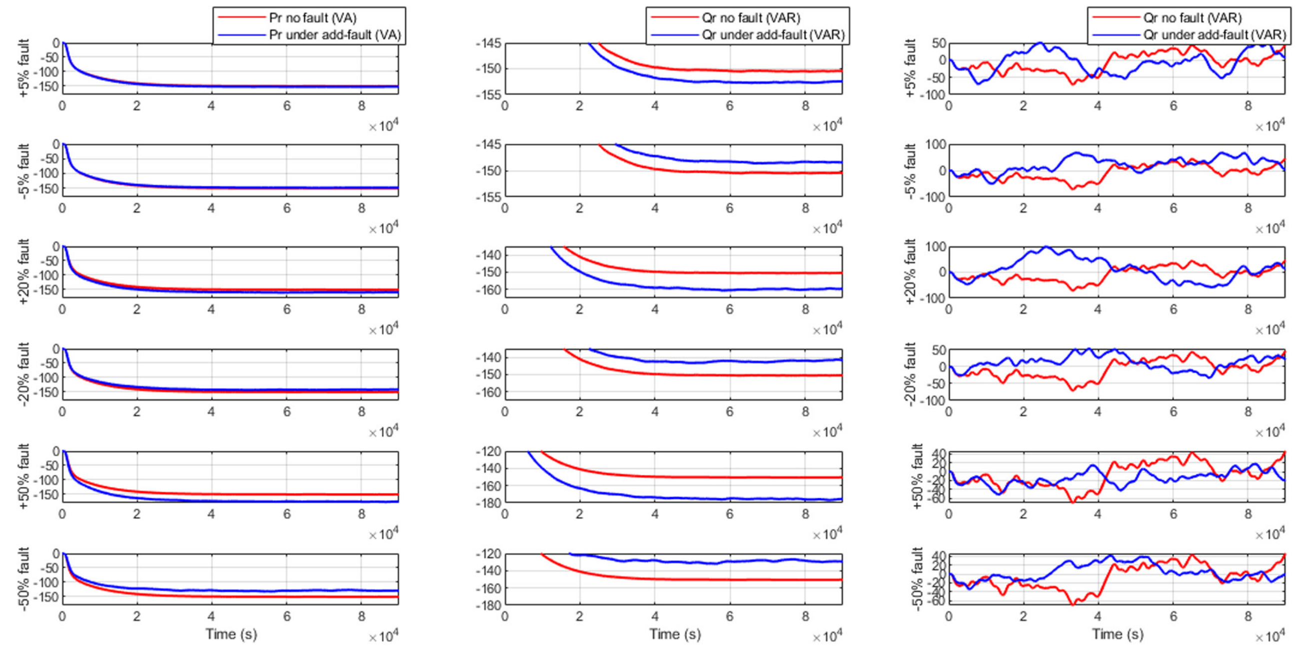

Fig. 25. Rotor active power and reactive power responses under rotor current sensor' faults.

TABLE III. STATISTICS OF KEY ELECTRICAL PARAMETERS UNDER ROTOR CURRENT SENSORS FAULTS

Electrical parameters	No Fault	−50%	−20%	−15%	−5%	+3%	+5%	+10%	+20%	+50%
Direct Rotor Current (A)	1	1.25	1.1	1.07	1.03	0.99	0.98	0.95	0.93	0.9
Quadrature Rotor Current (A)	3.5	4.35	3.75	3.7	3.6	3.45	3.4	3.35	3.25	3.1
Stator Active Power (VA)	101	75	90	95	100.5	101.5	102	103.5	105	107
Stator Reactive Power (VAR)	1150	1150	1150	1150	1150	1150	1150	1150	1150	1150
Grid Active Power (VA)	−103.85	−107.5	−105	−104.75	−104.25	−103.50	−103.45	−102.9	−102.5	−101
Grid Reactive Power (VAR)	−396	−405	−403.5	−403	−400	−395.5	−395	−397	−399	−390
Rotor Active Power (VA)	−150.45	−130	−142	−144.5	−147.5	−151.5	−152.5	−155	−160	−175

does not follow a consistent pattern with respect to fault type or phase, indicating sensitivity and instability to rotor current sensor faults.

IV. CONCLUSION

This paper investigates the behavior of a controlled grid-connected WECS based on DFIG under direct-quadrature rotor current sensor faults, including both additive and multiplicative disturbances affecting stator voltage, stator current, and rotor current sensors.

It was observed that faults in stator voltage and current sensors do not influence the direct-quadrature rotor current, whereas rotor current sensor faults significantly disturb the direct-quadrature rotor current, particularly at high fault magnitudes exceeding 50%. However, faults in those sensors do not influence the regulation of the DC-link voltage due to the RSC and GSC independency and decoupled in operation.

Stator voltage and current sensor faults have a minimal effect on grid voltage and active power but induce small perturbations in grid current and reactive power. These faults also affect stator current and reactive power without significantly altering stator active power. However, both types introduce notable disturbances in rotor voltage and reactive power and affect rotor current.

Rotor current sensor faults, on the other hand, have a clear impact on grid active and reactive power. They cause minimal changes in stator current and its corresponding powers but introduce significant disturbances in rotor voltage and reactive power and result in power imbalance across rotor phases.

Understanding these effects is essential in determining the most suitable FRT strategy for each fault type. Specifically, the severity and location of the fault guide whether a pure estimation, measurement-based, or hybrid compensation approach is more appropriate to maintain system reliability and performance. The choice of FRT strategy can be tailored as follows:

- For stator sensor faults (voltage or current), estimation-based compensation using observer schemes may be sufficient, as rotor feedback can help reconstruct the faulty stator signal indirectly.
- For rotor current sensor faults, a more robust FRT technique is required. This may involve hybrid strategies combining estimation and redundancy or even hardware-based redundancy in critical cases.
- When both converters are decoupled, the DC-link voltage is unaffected, indicating that FRT strategies can focus locally on affected subsystems rather than system-wide interventions.
- The insight contributes to the broader objective of developing effective FRT and FTC strategies for WECS based on DFIG, ensuring improved resilience, operational continuity, and reduced risk in the presence of sensor faults.

Data Availability Statement: The data that support the findings of this study are available on request from the corresponding author.

Peer-review: Externally peer reviewed.

Author Contributions: Concept – K.B., N.C.; Design – K.B., N.C., O.R.; Supervision – K.B., R.H., M.Z.; Resources – K.B., N.C.; Materials – K.B., N.C.; Data Collection and/ or Processing – K.B., N.C., O.R.; Analysis and/or Interpretation – N.C., O.R.; Literature Search – K.B., N.C., R.H., M.Z., O.R.; Writing – K.B., N.C.; Critical Review – K.B., N.C., R.H., M.Z., O.R.

Declaration of Interests: The authors have no conflicts of interest to declare.

Funding: The authors declare that this study received no financial support.

REFERENCES

1. A. M. Vural, and A. I. İsmail, "Modeling and control of an offshore wind farm connected to main grid with high voltage direct current transmission," *Electrica*, vol. 18, no. 2, pp. 198–209, 2018. [CrossRef]
2. K. E. Okedu, "Improved performance of doubly-fed induction generator wind turbine during transient state considering supercapacitor control strategy," *Electrica*, vol. 21006, pp. 198–210, 2022, 22:2. [CrossRef]
3. S. S. Sahou, K. Chatterjee, and P. M. Tripathi, "A coordinate control strategy using super-capacitor energy storage and series dynamic resistor for enhancement of fault ride-through of doubly fed induction generator," *Int. J. Green Energy*, vol. 16, no. 8, pp. 615–626, 2019. [CrossRef]
4. N. Z. Ibrahim, A. Al-Quteimat, M. Mozumdar, and S. Al-Jufout, "A novel approach for crowbar resistance determination for doubly fed induction generators in wind energy conversion systems," *Int. J. Ambient Energy*, vol. 43, no. 1, pp. 4102–4111, 2022. [CrossRef]
5. M. S. Chabani, M. T. Benchouia, A. Golea, and M. Becherif, "Finite-state predictive current control of a standalone DFIG-based wind power generation systems: Simulation and experimental analysis," *J. Control Autom. Electr. Syst.*, vol. 32, no. 5, pp. 1332–1343, 2021. [CrossRef]
6. M. Elmahfoud, B. Bossoufi, M. Taoussi, N. E. El Ouanjli, and A. Derouich, "Rotor field oriented control of doubly fed induction motor" International Conference on Optimization and Applications (ICOA), 2019. [CrossRef]
7. N. El Ouanjli, A. Derouich, A. El Ghzizal, A. Chebabhi, and M. Taoussi, "A comparative study between FOC and DTC control of the Doubly Fed Induction Motor (DFIM)" International Conference on Electrical and Information Technologies (ICEIT), 2017, p. 1–6. [CrossRef]

8. R. Tidke, and A. Chowdhury, "Quasi ZSI-fed sliding mode control-based indirect field-oriented control of IM using PI-fuzzy logic speed controller," *Electrica*, vol. 22, no. 1, pp. 70–83, 2021. [CrossRef]
9. I. Takahashi, and T. Noguchi, "A new quick-response and high-efficiency control strategy of an induction motor," *IEEE Trans. Ind. Appl.*, vol. IA–22, no. 5, pp. 820–827, 1986. [CrossRef]
10. T. Sutikno, N. R. N. Idris, and A. Jidin, "A review of direct torque control of induction motors for sustainable reliability and energy efficient drives," *Renew. Sustain. Energy Rev.*, vol. 32, pp. 548–558, 2014. [CrossRef]
11. M. El Mahfoud, B. Bossoufi, N. El Ouanjli, S. Mahfoud, and M. Taoussi, "Three speed controllers of direct torque control for a doubly fed induction motor drive–A comparison," *Electrica*, vol. 21, no. 1, pp. 129–141, 2021. [CrossRef]
12. R. Pena, J. C. Clare, and G. M. Asher, "Doubly fed induction generator using back-to-back PWM converters and its application to variable-speed wind-energy generation," *IEE Proc. Electr. Power Appl.*, vol. 143, no. 3, pp. 231–241, 1996. [CrossRef]
13. R. Cárdenas, R. Peña, J. Proboste, G. Asher, and J. Clare, "MRAS observer for sensorless control of standalone doubly fed induction generators," *IEEE Trans. Energy Convers.*, vol. 20, no. 4, pp. 710–718, 2005. [CrossRef]
14. A. Petersson, T. O. Thiringer, L. Harnefors, and T. A. Petru, "Modeling and experimental verification of grid interaction of a DFIG wind turbine," *IEEE Trans. Energy Convers.*, vol. 20, no. 4, pp. 878–886, 2005. [CrossRef]
15. P. Ledesma, and J. Usaola, "Doubly fed induction generator model for transient stability analysis," *IEEE Trans. Energy Convers.*, vol. 20, no. 2, pp. 388–397, 2005. [CrossRef]
16. B. H. Chowdhury, and S. Chellapilla, "Double-fed induction generator control for variable speed wind power generation," *Electr. Power Syst. Res.*, vol. 76, pp. 9–10, 786–800, 2006. [CrossRef]
17. B. Singh, and N. K. S. Naidu, "Direct power control of single VSC-based DFIG without rotor position sensor," *IEEE Trans. Ind. Appl.*, vol. 50, no. 6, pp. 4152–4163, 2014. [CrossRef]
18. L. Xu, "Coordinated control of DFIG's rotor and grid side converters during network unbalance," *IEEE Transactins Power Electron.*, vol. 23, pp. 1041–1049, 2008. [CrossRef]
19. A. Balogun, O. Ojo, and F. Okafor, "Decoupled direct control of natural and power variables of doubly fed induction generator for extended wind speed range using feedback linearization," *IEEE J. Emerg. Sel. Top. Power Electron.*, vol. 1, no. 4, pp. 226–237, 2013. [CrossRef]
20. A. A. Ansari, and G. Dyanamina, "Fault ride-through operation analysis of doubly fed induction generator-based wind energy conversion systems: A comparative review," *Energies*, vol. 15, no. 21, p. 21, 8026, 2022. [CrossRef].
21. Q. Huang, X. Zou, D. Zhu, and Y. Kang, "Scaled current tracking control for doubly fed induction generator to ride-through serious grid faults," *IEEE Trans. Power Electron.*, vol. 31, no. 3, pp. 2150–2165, 2016. [CrossRef]
22. R. Zhu, Z. Chen, X. Wu, and F. Deng, "Virtual damping flux-based LVRT control for DFIG-based wind turbine," *IEEE Trans. Energy Convers.*, vol. 30, no. 2, pp. 714–725, 2015. [CrossRef]
23. D. Zhu, X. Zou, S. Zhou, W. Dong, Y. Kang, and J. Hu, "Feedforward current references control for DFIG-based wind turbine to improve transient control performance during grid faults," *IEEE Trans. Energy Convers.*, vol. 33, no. 2, pp. 670–681, 2018. [CrossRef]
24. J. Bhukya, and V. Mahajan, "Optimization of damping controller for PSS and SSSC to improve stability of interconnected system with DFIG based wind farm," *Int. J. Electr. Power Energy Syst.*, vol. 108, pp. 314–335, 2019. [CrossRef]
25. M. J. Hossain, T. K. Saha, N. Mithulananthan, and H. R. Pota, "Control strategies for augmenting LVRT capability of DFIGs in interconnected power systems," *IEEE Trans. Ind. Electron.*, vol. 60, no. 6, pp. 2510–2522, 2013. [CrossRef]
26. M. J. Hossain, H. R. Pota, V. A. Ugrinovskii, and R. A. Ramos, "Simultaneous STATCOM and pitch angle control for improved LVRT capability of fixed speed wind turbines," *IEEE Trans. Sustain. Energy*, vol. 1, no. 3, pp. 142–151, 2010. [CrossRef]
27. R. Suryana, "Frequency control of standalone wind turbine with supercapacitor," In 33rd International Telecommunications Energy Conference (INTELEC), Amsterdam, Netherlands: IEEE Publications 2011, 2011, pp. 1–8. [CrossRef]
28. R. Aghatehrani, R. Kavasseri, and R. C. Thapa, "Power smoothing of the DFIG wind turbine using a small energy storage device," In *IEEE Power Energy Soc. Gen. Meet.* MN, USA: IEEE Publications, pp. 1–6, 2010. [CrossRef]
29. S. Alepuz, A. Calle, S. Busquets-Monge, S. Kouro, and B. Wu, "Use of stored energy in PMSG rotor inertia for low-voltage ride-through in back-to-back NPC converter-based wind power systems," *IEEE Trans. Ind. Electron.*, vol. 60, no. 5, pp. 1787–1796, 2013. [CrossRef]
30. P. Chen, D. Han, and K. C. Li, "Robust adaptive control of maximum Power Point tracking for wind power system," *IEEE Access*, vol. 8, pp. 214538–214550, 2020. [CrossRef]
31. S. M. Barakati, M. Kazerani, and J. D. Aplevich, "Maximum power tracking control for a wind turbine system including a matrix converter," *IEEE Trans. Energy Convers.*, vol. 24, no. 3, pp. 705–713, 2009. [CrossRef]
32. M. Karabacak, L. M. Fernandez-Ramirez, T. Kamal, and S. Kamal, "A New Hill climbing maximum power tracking control for wind turbines with inertial effect compensation," *IEEE Trans. Ind. Electron.*, vol. 66, no. 11, pp. 8545–8556, 2019. [CrossRef]
33. M. Abbas, H. Chafouk, and S. A. E. M. Ardjoun, "Fault diagnosis in wind turbine current sensors: Detecting single and multiple faults with the extended Kalman Filter bank approach," *Sensors (Basel)*, vol. 24, no. 3, p. 728, 2024. [CrossRef]
34. Y. Mousavi, *Optimal and Robust Fault Tolerant Control of Wind Turbines Working under Sensor, Actuator, and System Faults*. arXiv preprint, arXiv:2308.12550, 24, 2023.
35. A. U. Rehman *et al.*, "Fault detection and fault severity calculation for rotor windings based on spectral, wavelet and ratio computation analyses of rotor current signals for a doubly fed induction generator in wind turbines," *Electr. Eng.*, vol. 102, no. 3, pp. 1091–1102, 2020. [CrossRef]
36. Y. Wenxin, D. Jiang, J. Wang, R. Li, and L. Yang, "Rotor-current-based fault detection for doubly-fed induction generator using new sliding mode observer," *Trans. Inst. Meas. Control*, pp. 1–13, 2020. [CrossRef]
37. J. Mohammadi, S. Vaez-Zadeh, S. Afsharnia, and E. Daryabeigi, "A combined vector and direct power control for DFIG-Based wind turbines," *IEEE Trans. Sustain. Energy*, vol. 5, no. 3, pp. 767–775, 2014. [CrossRef]
38. K. S. Xiahou, Y. Liu, M. S. Li, and Q. H. Wu, "Sensor fault-tolerant control of DFIG based wind energy conversion systems," *Int. J. Electr. Power Energy Syst.*, vol. 117, 105563, 2020. [CrossRef].
39. U. S. Sabura Banu, and G. Uma, "Fault Tolerant control of CSTR with ANFIS based dedicated observer and state feedback control using linear quadratic regulator under abrupt sensor failure conditions," *Instrum. Sci. Technol.*, vol. 37, no. 1, pp. 61–81, 2009. [CrossRef]
40. G. You, T. Xu, H. Su, X. Hou, and J. Li, "Fault-tolerant control for actuator faults of wind energy conversion system," *Energies*, vol. 12, no. 12, p. 12, 2350, 2019. [CrossRef]
41. A. G. Abo-Khalil, "Grid connection control of DFIG in variable speed wind turbines under turbulent conditions," *Int. J. Renew. Energy Res.*, vol. 9, no. v9i3, p. 3, 2019. [CrossRef]
42. C. Dufour, and J. Belanger, "A real-time simulator of doubly fed induction generator based wind turbine applications. IEEE" 35th Annual Power Electronics Specialists Conference, Aachen, Germany 2004, 2004, pp. 3597–3603. [CrossRef]
43. A. A. Tanvir, A. Merabet, and R. Beguenane, "Real-time control of active and reactive power for doubly fed induction generator (DFIG)-based wind energy conversion system," *Energies*, vol. 8, no. 9, pp. 10389–10408, 2015. [CrossRef]
44. K. Beddek, A. Merabet, M. Kesraoui, A. A. Tanvir, and R. Beguenane, "Signal-based sensor fault detection and isolation for PMSG in wind energy conversion systems," *IEEE Trans. Instrum. Meas.*, vol. 66, no. 9, pp. 2403–2412, 2017. [CrossRef]

Naziha Chouider received her M.Sc. degree in Automation and Control Engineering from the Institute of Electrical and Electronic Engineering (IEEE ex-INELEC), M'Hamed Bougara University of Boumerdes, Boumerdes, Algeria, in July 2022, where she is currently pursuing the Ph.D. degree in engineering in the Faculty of Hydrocarbons and chEmistry. She is a research member at the Laboratory of Applied Automation, her current research interests include renewable energy conversion systems, control and automation, faults detection and diagnosis.

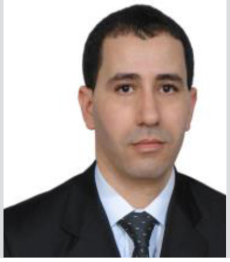

Karim Beddek received the Ph.D. degree in Electrical Engineering from the University of M'Hamed Bougara Boumerdes, Boumerdes, Algeria and Saint Mary's University, Halifax, NS, Canada in 2017. He is currently an Associate Professor with the Department of Automation and Electrification, Faculty of Hydrocarbons and Chemistry, M'Hamed Bougara University of Boumerdes. His current research interests include renewable (wind–solar) energy conversion systems, energy management, advanced control systems, and smart grid.

Rezki Haddouche received the Ph.D. degree in Electrical Engineering from the University of M'Hamed Bougara Boumerdes,Boumerdes, Algeria in 2018. He is currently an Associate Professor with the Department of power and control, Institute of Electrical and Electronic Engineering, M'Hamed Bougara University of Boumerdes. His current research interests include wind energy conversion systems and control of dynamic systems.

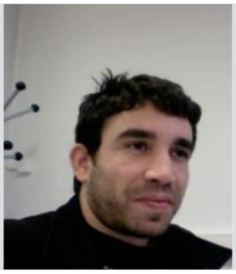

Mohamed Zerrougui received the Ph.D. in Automatic Control from the University Henri Poincaré, Nancy, France, in 2011. Following this, he pursued a post-doctoral position at the University Libre de Bruxelles between 2012 and 2013. He is currently an Associate Professor with the Laboratoire d'Informatique et des Systèmes at the University of Aix-Marseille. His research interests encompass a diverse array of topics including nonlinear systems, state observers, observer-based control, robustness and their application in renewable energy processes and robotics.

Omar Ramdani obtained his Engineer degree in Automation Engineering from the Faculty of Hydrocarbons and Chemistry at the University of M'Hamed Bougara Boumerdes, Boumerdes, Algeria, in 2010. Currently pursuing a Ph.D degree at the same university, he is a dedicated research member of the Laboratory of Applied Automation. His expertise spans renewable energy conversion systems, machine learning applications, and fault detection and diagnosis.

APPENDIX

Table I. System Parameters

QUANTITY	Value
DFIG Machine	
Power	2000W
Stator’s Voltage	120V
Rotor’s Voltage	360V
Stator’s Current	10A
Rotor’s Current	3.3A
Speed	1800RPM
Pole-Pairs	2
Stator’s Inductance	0.0662
Rotor’s Inductance	0.0662
Mutual Inductance	0.0945
Dynamometer Machine	
Three Phase Required Voltage	208V
Three Phase Required Current	12A
Speed Range	0-360RPM
IGBT Inverter	
DC Voltage	420V
DC Current	10A
Switching Frequency	0-20kHz

GSC gains
Kp = 0.5 Ki = 7 Iregulator = 0.0001A
RSC gains
Kp = 4.5 Ki = 7.5

W = Watt, V = Volt, A = Ampere, RPM = Round Per Minute, Hz =Hertz